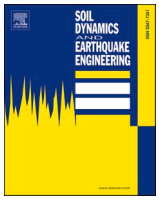
Soil Dynamics and Earthquake Engineering 173 (2023) 108089



Contents lists available at ScienceDirect

Soil Dynamics and Earthquake Engineering

journal homepage: www.elsevier.com/locate/soildyn



Characterization and modeling of ground motion at depth in soft sedimentary rocks: Application to the Swiss Molasse Basin

Miroslav Hallo [a,*], Afifa Imtiaz [b], Maria Koroni [b], Vincent Perron [c], Donat Fäh [d]

[a] Swiss Seismological Service, ETH Zurich, Building NO, Room H60, Sonneggstrasse 5, 8092, Zürich, Switzerland
[b] Swiss Seismological Service, ETH Zurich, Building NO, Room H55, Sonneggstrasse 5, 8092, Zürich, Switzerland
[c] French Alternative Energies and Atomic Energy Commission, Saint-Paul-les-Durance, France
[d] Swiss Seismological Service, ETH Zurich, Building NO, Room H53.1, Sonneggstrasse 5, 8092, Zürich, Switzerland

ARTICLE INFO

Keywords:
Ground motion at depth
Strong ground motion
Peak ground acceleration
Site-specific seismic hazard
Surface-borehole transfer function
S/B spectral ratio
Swiss Molasse Basin
Broadband seismic waveforms
Deep geological disposal
Nuclear waste repository

ABSTRACT

The level of earthquake motion observed on the ground surface differs from the shaking at locations buried at a depth. Characterization of the underground shaking is important for the local seismic hazard assessment at depth which is an insufficiently investigated topic so far. Advancements in the prediction of the ground motion at depth are especially important for the design of deep geological disposals of nuclear waste, buildings with deep foundations, or studies focused on soil-structure interactions. In this paper, we analyze site-specific transfer functions that relate ground motions on the surface to that at a depth at sites located within soft sedimentary rocks of the Swiss Molasse Basin. We first evaluate empirical surface-to-borehole amplification functions at six borehole sites, compare them with predictions by a theoretical model, and characterize the high-frequency surface-to-borehole amplification. Next, we perform full-waveform prediction of ground motion at depth from surface recordings of seven significant regional earthquakes with $M_L > 4$. The comparison of predicted and observed acceleration waveforms shows a high level of similarity in a broad frequency range and well-predicted values of PGA, PGV, and response spectra. Finally, we model a scenario earthquake for 9975 years return period at a test site, and we predict associated broadband waveforms at depth. By the latter, we demonstrate that our method to predict ground motions at depth can be used as a basis for the site-specific seismic hazard of deep geological disposals of nuclear waste.

1. Introduction

The characterization of site-specific earthquake ground motion is the basic element of local seismic hazard assessment. An accurate prediction of ground motion is especially important for the earthquake-resistant design of structures of special importance (e.g., hospitals, fire stations, dams, power plants, and deep geological disposal sites). In such cases, the seismic hazard is evaluated for long return periods and should take into account the effects of near-surface geology around the foundation of the structure. The near-surface rock and soil layers cause amplification of seismic waves that can be approximated by using soil classes [1,2]; nevertheless, such a procedure is not applicable to underground sites buried at a depth. Therefore, methods to characterize and predict the ground motion at depth need to be developed for important structures like nuclear waste repositories or critical infrastructure buildings with deep foundations. So far, the prediction of the ground motion at depth is an insufficiently investigated topic, which underlines the importance of this paper.

Theoretical predictions of ground motions caused by earthquakes can be performed by modeling approaches based on various determin-

Abbreviations: BBP, Broadband Platform; CAV, Cumulative absolute velocities; CEN, European Committee for Standardization; ED, Envelope delay; ENSI, Swiss Federal Nuclear Safety Inspectorate; ESD, Energy spectral density; ETH, Swiss Federal Institute of Technology; LFM, Lower Freshwater Molasse; LMM, Lower Marine Molasse; NAGRA, National Cooperative for the Disposal of Radioactive Waste; PGA, Peak ground acceleration; PGV, Peak ground velocity; PPD, Posterior probability density; S/B, Surface-to-borehole; SCEC, Southern California Earthquake Center; SDSNet, Swiss Digital Seismic Network; SED, Swiss Seismological Service; SIA, Swiss Society of Engineers and Architects; SM, Stochastic model; SNR, Signal-to-noise ratio; SSMNet, Swiss Strong Motion Network; TF, Transfer function; UFM, Upper Freshwater Molasse; UMM, Upper Marine Molasse.

* Corresponding author.
E-mail addresses: miroslav.hallo@sed.ethz.ch (M. Hallo), afifa.imtiaz@sed.ethz.ch (A. Imtiaz), maria.koroni@sed.ethz.ch (M. Koroni), vincent.perron@cea.fr (V. Perron), donat.faeh@sed.ethz.ch (D. Fäh).

https://doi.org/10.1016/j.soildyn.2023.108089
Received 8 February 2023; Received in revised form 13 June 2023; Accepted 14 June 2023
0267-7261/© 2023 The Authors. Published by Elsevier Ltd. This is an open access article under the CC BY license (http://creativecommons.org/licenses/by/4.0/).

istic or stochastic numerical methods (e.g., [3–9]). The earthquake source is usually described by the slip-rate function on a fault or the frequency content of radiated seismic waves (e.g., [10–12]). The path term is mainly governed by the mechanical properties of the bedrock, i.e., seismic velocity, geometrical spreading, and intrinsic and scattering attenuation (e.g., [13,14]). Finally, the site term represents the site-specific response to incident seismic waves. The site response can be modeled deterministically, approximated using average shear-wave (S-wave) velocity to the depth of 30 m (v_{S30}) or site-condition proxies (e.g. [15]), or expressed by a complex-valued transfer function (TF) in the spectral domain [16].

The TF relates ground motions on the soil surface to that at a reference point by a spectral ratio [17–19]. The reference point can be assumed to be on the outcropping rock or in a borehole buried at depth. The characterization of ground motion at depth is complicated by the interference of up-going and down-going waves reflected by the surface [19,20]; hence, the surface-borehole TF consists of their constructive and destructive interferences (e.g., [21,22]). We would like to emphasize that the surface-to-borehole amplification differs in amplitudes and frequencies of resonance peaks from the surface-to-outcrop amplification that is standardly evaluated on the ground surface. When considering 1D stratigraphy, the surface-borehole TF can be evaluated as a solution to the wave equation in the 1D medium of horizontal viscoelastic homogeneous layers (e.g., [23,24]); or, more preferably, by using the stochastic model (SM) introduced by [25] that is described in the following section. The modeling is more challenging in the case of a site characterized by 2D or 3D resonance effects (e.g., [26]); however, these sites are often in distinctive valleys and can be identified by, e.g., the single-station approach following [27].

Similar to that on the ground surface, earthquake shaking at depth can be quantitatively characterized by the peak ground acceleration (PGA), peak ground velocity (PGV), response spectra, cumulative absolute velocities (CAV), or Arias intensity (I_A) measures [28–30]. However, it is advantageous to model full broadband seismic waveforms as all the aforementioned parameters can be derived from them [31]. The broadband waveforms at depth can be predicted analytically from surface observations by the deconvolution method if the surface-borehole TF is given (e.g., [23]). For instance, the 1D TF deconvolution analysis was performed by [32] to characterize motions at the foundation level of nuclear power plants in the USA, and by [25] to compare observed and theoretical waveforms at depth in borehole monitoring arrays in Japan. Predictions of waveforms at depth from surface observations are rare and limited to already recorded significant earthquakes, while predictions from synthetic waveforms, which are also introduced in this paper, may provide insight into ground motions expected in the future. The latter is especially important for long return periods, required by earthquake-resistant design standards for structures of special importance.

In this paper, we extend and apply the surface-borehole SM method proposed by [25] to soft rock sites in the Swiss Molasse Basin [33]. This modeling method is preferred as it accounts for random spatial variations of rock properties and it produces realistic surface-borehole TFs in a broad frequency range. For our application, a modification of the method is necessary in order to consider the effects caused by soft rocks at the depth of our interest. In particular, the empirical surface-borehole TF may be influenced by lithological interfaces below the borehole sensor if they have a significant impedance contrast [34]. Therefore, we extend the method to model the ground motion at depth inside soft sedimentary rocks (i.e., sandstones, conglomerates, mudstones, marls, or clays), where we expect an interface with a significant impedance contrast close below the reference point at depth.

We first evaluate empirical surface-to-borehole (S/B) amplification functions at six borehole sites in Switzerland and compare them with theoretical predictions by the surface-borehole SM. We also perform inversion of empirical amplification functions to infer and validate local S-wave velocity models. Next, we perform the deconvolution of ground motions at depth from surface recordings of the 2017 Urnerboden M_w4.1 earthquake [35] and another six significant regional earthquakes. The comparison of observed and predicted waveforms validates our characterization of ground motions at depth in soft sedimentary rocks. Finally, we model synthetic broadband waveforms for the M_w4.1 Urnerboden earthquake as a validation, and we model a scenario earthquake for 9975 years return period including the prediction at depth for demonstration purposes. The utilized M_w5.8 earthquake scenario is the dominant event from disaggregation of the Swiss seismic hazard model SUIhaz15 [36,37].

2. Methods

2.1. Transfer function

Let us start with a common definition of the surface-borehole TF by using the spectral ratio. First, we assume two one-component seismic waveforms of the same origin that are observed on the ground surface $y_S(t)$ and in a borehole $y_B(t)$, in which t denotes time. The Fourier transform of these real-valued functions yields complex-valued spectral functions $Y_S(f)$ and $Y_B(f)$, in which f is frequency. The surface-borehole TF is then expressed as

$$H(f) = \frac{Y_S(f)}{Y_B(f)}, \tag{1}$$

in which $H(f)$ is the complex-valued TF in the spectral domain. The absolute value of the TF, i.e. $|H(f)|$, is equal to the S/B ratio of the amplitude spectrum, which is the S/B amplification function [16].

The TF can be determined from seismic waveforms observed by vertical monitoring arrays in boreholes (i.e., empirical TF) or computed by a numerical modeling technique (i.e., theoretical TF). Based on the pioneering work by [38]; the surface-borehole TF can be modeled as a linear, equivalent linear, or nonlinear response of the 1D medium of horizontal homogeneous layers (e.g., [23]). The linear response is sufficient for modeling small-strain effects; otherwise, equivalent linear or nonlinear response modeling should be considered (e.g., [39]). In this work, the linear response of damped layers on the base rock is solved numerically by evaluating recursion formulas in all layers above the reference point (e.g., [23]).

2.2. Stochastic model

The classical TF modeling method relies on the response of the 1D medium of horizontal viscoelastic homogeneous layers, while real near-surface layers are rather heterogeneous with rough interfaces and complex site response [40]. Indeed, it is emphasized by numerous studies that considering a velocity gradient or heterogeneities may improve the mutual fit between empirical and theoretical TFs (e.g., [22,41,42]). Moreover, surface-borehole TFs modeled in 1D layered media exhibit distinctive amplitudes of resonance peaks that are not observed in empirical data. To overcome these issues [25], proposed a stochastic model (SM) which predicts more realistic surface-borehole site responses.

To construct the SM, a set of random 1D media is generated from the reference S-wave velocity model that is given *a priori*. Random draws are log-normally distributed with a mean of the reference model and a standard deviation given by a percentage (following recommendations by [25]; 15% is used in this study). The medium damping and layer thicknesses are randomized as well. The reference damping model is introduced through the quality factor for S-waves, which is approximated to be one-tenth of the S-wave velocity in m/s [43,44]. Next, surface-borehole TFs are solved numerically for all prepared 1D media and the ensemble of TFs is used to compute respective energy spectral density (ESD) and envelope delay (ED) functions. The S/B ESD function $L(f)$ is defined as

$$L(f) = 10 \log_{10}|H(f)|^2 \ [\mathrm{dB}], \tag{2}$$

in which dB indicates the unit in decibels. This function determines S/B amplification in the logarithmic scale. The surface-borehole ED function $\tau(f)$, defined by [25]; expresses the difference between the first derivatives of surface and borehole phase spectra as

$$\tau(f) = \frac{1}{2\pi}\frac{\mathrm{d}\varphi(f)}{\mathrm{d}f}, \tag{3}$$

in which $\varphi(f)$ is the unwrapped phase spectrum of $H(f)$. The surface-borehole ED has units of time and meaning of the harmonic delay between surface and borehole envelopes. Finally, the SM is defined by a pair of coupled $\overline{L}(f)$ and $\overline{\tau}(f)$ spectral curves representing an average from all realizations within the ensemble of TFs (the overline denotes average values). The SM is rid of artificial spikes of resonance peaks and it resembles empirical surface-borehole TFs. For details about the SM, the reader is referred to [25].

2.3. Predictive transfer function

In the SM, the pair of coupled $\overline{L}(f)$ and $\overline{\tau}(f)$ spectral curves characterize the theoretical site response. These functions can be used for the reconstruction of the complex-valued TF by using the exponential form of complex numbers and equations (2) and (3). Following [25]; the predictive TF $\widehat{H}(f)$ is expressed, after some trivial algebraic operations, as

$$\widehat{H}(f) = \sqrt{10^{0.1\overline{L}(f)}}\exp\left(i2\pi\int\overline{\tau}(f)\,\mathrm{d}f\right), \tag{4}$$

in which i is the imaginary unit and the hat symbol denotes predicted values. Then, the $\widehat{H}(f)$ can be substituted for $H(f)$ into equation (1), which leads to an exact mathematical relation between surface and borehole Fourier spectra. This relation allows us to compute the prediction of a unique Fourier spectrum at depth if a surface waveform is available. The resultant deconvolved waveform at depth is the inverse Fourier transformation of the predicted spectrum.

2.4. Inversion of empirical amplification

Vertical monitoring arrays in boreholes allow us to measure empirical surface-borehole TFs. These empirical S/B amplification functions can be used in an inversion procedure to retrieve the local S-wave velocity model. For this purpose, we utilize the inversion method by [25] formulated in the Bayesian probabilistic framework (e.g., [45]). This inversion method uses the SM as the forward problem solver and it utilizes random sampling by the Metropolis-Hastings algorithm [46] coupled with the parallel tempering technique [47]. The inversion result is the posterior probability density (PPD) that expresses the probability of model parameter values (i.e., S-wave velocity, depth of layer interfaces, and medium damping). Therefore, the PPD includes information about the solution uncertainty. This inversion uses solely amplification data; hence, it is sensitive to velocity contrasts between layers rather than absolute values of the S-wave velocity.

2.5. Broadband waveform modeling

To perform modeling of synthetic surface waveforms at a broadband frequency range, we use software developed by the Southern California Earthquake Center (SCEC) [48]. This SCEC Broadband Platform (BBP) is developed to perform physics-based ground motion simulations and it has been thoroughly validated [49,50]. In our research, we apply the hybrid modeling method by [8,51] that is implemented in the BBP.

The method by [51] models three-component broadband acceleration waveforms at two different ranges of frequencies. The low-frequency part (<1 Hz) is calculated deterministically for a given Earth structure and source model, while the high-frequency part (1–100 Hz) is modeled by the stochastic approach. The BBP first generates a random distribution of the heterogeneous slip on a given fault plane. The propagation of low-frequency elastic waves is modeled by using Green's functions. We computed our own Green's functions in a suitable regional 1D velocity model (see Appendix A) using the frequency-wavenumber method by [52]. Regarding the site term, the BBP uses a rather simplified approach by using v_{S30} adjustments. Still, it is a well-validated approach and should result in reliable broadband waveforms. We would like to emphasize that v_{S30} adjustments are used only inside the BBP for the modeling of synthetic broadband waveforms on the ground surface, and not elsewhere within this paper.

The method implemented in BBP is intended to model waveforms of large earthquakes dominated by S-waves; hence, it does not produce high-frequency pressure-wave (P-wave) signals. On the other hand, P-waves are non-negligible in the case of small-to-moderate earthquakes, which further requires their proper modeling (e.g., [53]). Because of that, we model high-frequency P-wave waveforms using the nonstationary stochastic method introduced by [54] and add them to broadband waveforms produced by the BBP. The stochastic P-wave waveforms are scaled to have a maximal amplitude five times smaller than S-waves and the duration of the P-wave packet about 25% longer than in the original method. As a result, our modeled broadband waveforms include deterministic low- and stochastic high-frequency parts of both P- and S-wave phases.

3. Characterization of Swiss sites

In this section, we evaluate empirical surface-borehole TFs from borehole-monitoring arrays in Switzerland and compare them with theoretical predictions by the surface-borehole SM. The locations of six selected borehole arrays and earthquake epicenters from the period 2013–2021 are shown in Fig. 1. Significant earthquakes with local magnitude $M_L > 4$ (purple circles) are summarized in Table 1.

First, borehole-monitoring arrays BOBI, HAMIK, and STIEG are part of a monitoring system for the planned nuclear waste repository in Switzerland financed by the National Cooperative for the Disposal of Radioactive Waste (NAGRA). They are equipped with seismometers on the ground surface and at depths of 153, 139, and 123 m, respectively. The depth of these boreholes is not sufficient to reach the crystalline basement; hence, borehole sensors are placed in the soft sedimentary rocks of the Swiss Molasse Basin. For these sites, site characterization was performed and S-wave velocity profiles were measured [55]. These velocity profiles will be provided later in this section. Next, borehole sites ROMAN and WOLEN are part of the Swiss Digital Seismic Network (SDSNet) and are equipped with sensors at depths of 98 and 133 m, respectively. These two sites are of secondary importance for this paper's purpose; hence, the detailed characterization is present only in Appendix B. The last selected borehole site SVISP is a part of the Swiss Strong Motion Network (SSMNet). The lithology at this site differs from previous ones as it is located in the Rhone valley which is filled with unconsolidated alluvial, glaciolacustrine, and moraine deposits [56]. The borehole is instrumented with seismometers at three different depths; but in our analysis, we use only the deepest sensor at 102 m depth.

3.1. Empirical surface-borehole TFs

To determine empirical surface-borehole TFs, we use seismic waveforms recorded by the vertical monitoring arrays in the years 2013–2021. The selected waveforms are recordings of local earthquakes with hypocenter depths less than 35 km having M_L in the range of 1.5–4.6 (see Fig. 1a). The strongest earthquake in the database is the 2017 Urnerboden M_L4.6 (M_w4.1) earthquake, which had the largest instrumentally recorded PGA of 85 cm/s^2 measured on rockslide

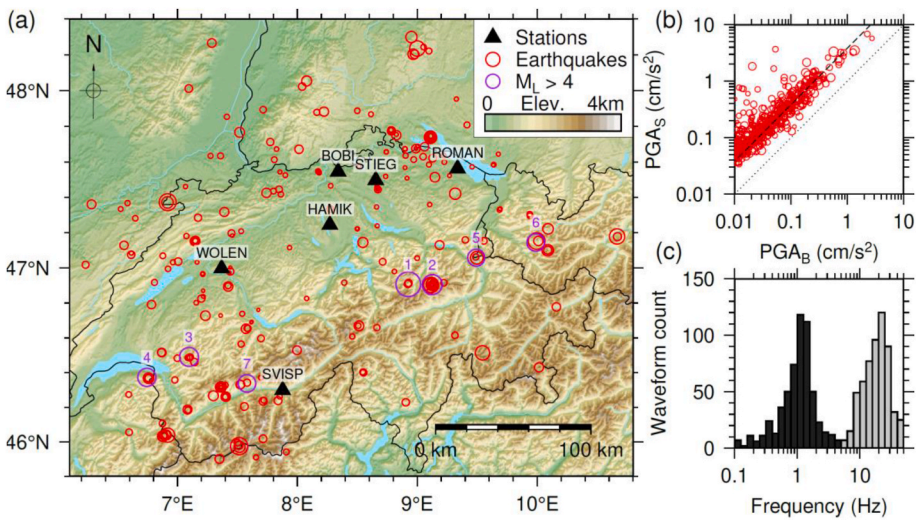


Fig. 1. Selected earthquakes and borehole-monitoring arrays in Switzerland. The map in (a) shows the location of earthquake epicenters (red and purple circles) and monitoring boreholes (black triangles). Earthquakes have magnitudes $1.5 < M_L < 4.6$ and hypocenter shallower than 35 km. (b) shows the dependency between PGA values measured on the ground surface (PGA_S) and in the borehole (PGA_B) for all event-borehole pairs. The regression model determined using the linear least squares is shown by the black dashed line. (c) displays a histogram of low- and high-frequency bounds of the useful signal (black and gray bars, respectively).

Table 1
List of earthquakes with $M_L > 4$.

N.	M_L	Date	UTC	Location	Lat. (deg)	Lon. (deg)	Depth (km)	Epicentral dist. (km)
#1	4.6	2017/03/06	20:12:07	Urnerboden	46.91	8.93	4	62–118
#2	4.3	2020/10/25	19:35:43	Elm	46.90	9.12	1	74–133
#3	4.3	2017/07/01	08:10:34	Chateau-d'OEx	46.49	7.10	4	60–123
#4	4.2	2019/05/28	08:48:05	Montreux	46.37	6.75	4	150
#5	4.1	2013/12/12	00:59:18	Sargans	47.06	9.49	6	79
#6	4.1	2018/01/17	19:07:19	Montafon	47.15	9.99	1	67–187
#7	4.1	2016/10/24	14:44:11	Leukerbad	46.34	7.58	8	23–114

deposits in the Linthal village [35]. North-south and east-west horizontal components were rotated into transverse components and further processed following the procedure described by [25]. The quantitative comparison between transverse component PGA measured on the ground surface (PGA_S) and in the borehole (PGA_B) is shown in Fig. 1b. This comparison shows systematically higher values of PGA measured on the ground surface than in 98–153 m deep boreholes, which can be approximated by the linear relation $PGA_S \cong 3.84\ PGA_B$ for the six selected downhole arrays in Switzerland (a solution of the linear least squares).

The earthquake signal could be below a local noise level for some event-sensor pairs, especially at low and very high frequencies. To ensure that we analyze only a spectrum of the useful signal, we determine low- and high-frequency bounds between which the amplitude spectrum has a signal-to-noise ratio (SNR) above three. These bounds are determined and manually adjusted for all waveforms individually. A statistic of the final bandwidths of the useful signal is shown in Fig. 1c. Next, each pair of waveforms observed on the ground surface and in the borehole is processed to obtain S/B amplification and surface-borehole ED curves. The derivatives of phase spectra are determined using the method by [57]; and individual spectral curves are smoothed by using the Konno-Ohmachi algorithm with parameter $b = 80$ [58]. Finally, the median curve from all available empirical spectral curves represents the empirical surface-borehole TF. These empirical TFs are complemented with 16th and 84th percentiles (i.e., inter-event variability).

3.2. Geological settings

Most of the sites under consideration in this study are located in the Swiss Molasse Basin [33]. It is a foreland basin between the Jura Mountains in the north and the Alps in the south. The thickness of this typically wedge-shaped basin decreases from about 4 km in the south to a few hundred meters in the north. The crystalline basement is formed by Precambrian rocks, which are overlain by the Mesozoic units consisting of shallow marine carbonates. As the Quaternary sediments are generally quite thin, the geology of this area is rather dominated by the thick Tertiary sequence, which originates from the erosion of the Alps. Lithostratigraphically, the Tertiary unit is divided into four main formations depending on marine or continental sedimentary facies: Lower Marine/Freshwater Molasse (LMM/LFM) and Upper Marine/Freshwater Molasse (UMM/UFM). The LMM is formed during the early Oligocene age and it consists of fine-grained shallow marine sandstones, clays, and marls. The LFM of the late Oligocene-early Miocene age consists of medium-to-coarse-grained fluviatile sandstones, marls, fan conglomerates, and breccias. The overlying UMM, formed during the early Miocene, consists of fine-to-medium-grained marine sandstones, marls, and coastal conglomerates. The topmost part is formed of the UFM of the middle-late Miocene age, consisting of fluviatile sandstones, silty marls, bentonites, and fan conglomerates.

At the BOBI site, a borehole log and a nearby site characterization measurement [59] are available. The surface station is located on the top of a large moraine deposit and the upper 26 m of the subsurface is characterized as Pleistocene gravel with weathered topsoil. UMM and LFM formations are observed at depths of 26–52 m and 52–120 m, respectively. The deepest part (120–160 m) of the borehole is characterized by the Malm unit (Upper Jurassic). The borehole profile and nearby site characterization at the HAMIK site [60] show a 110 m thick cover of Quaternary deposits overlying the UFM at 110–145 m depth. The borehole log and the site characterization at the STIEG station [61] indicate a 2 m thin layer of Quaternary deposits overlying the UFM at a depth of 2–130 m. The topmost bedrock units below these three stations probably consist of marine and fluvial deposits of Oligocene and Miocene age, mostly sandstone and conglomerates intercalated with clay and marl layers of variable thickness and consolidation [55]. It is perceivable that the largest impedance contrast at these sites will depend on the lithology of the base of the Tertiary and the level of

erosion of Jurassic and Cretaceous formations underneath.

No site characterization is available for the next sites WOLEN and ROMAN. The WOLEN site is located in the central part of the Swiss Molasse Basin. From a nearby geological cross-section [62], it can be inferred that it is characterized by a 50–75 m thick layer of unconsolidated deposits, overlying a thick (>200 m) LFM layer. The ROMAN site is located on the northeast edge near Lake Constance. From a nearby geological cross-section [63], it can be inferred that an approximately 10–20 m thick layer of unconsolidated deposits overlies a thick (>200 m) UFM unit at this site.

3.3. Results for NAGRA sites

The empirical surface-borehole TFs at NAGRA borehole sites (i.e., BOBI, HAMIK, and STIEG) are shown by black curves in Fig. 2. There are four-to-six noticeable S/B amplification peaks and EDs indicate good data quality between approximately 1 and 30 Hz, where they have expected values and acceptable scatter. Such a reliable frequency range is consistent with the histogram of useful-signal bands shown in Fig. 1c.

Next, theoretical S/B amplification curves (i.e., surface-borehole SMs) were computed using the linear response of a reference 1D medium. The site-specific reference velocity models originate from site characterization measurements [55,64]. The surface-borehole SMs were first computed as the response of the medium above the borehole sensor depth indicated as 'SM reference (upper)' in Fig. 2. In such a scenario, the borehole reference point is located in a hard rock (i.e., a rigid half-space) that does not influence the S/B amplification by itself. However, it is not a valid assumption in this case as frequencies of observed and predicted amplification peaks do not match at all (light-blue curves in Fig. 2). Indeed, NAGRA borehole sensors are placed within soft sedimentary rocks that are likely underlain by a harder rock. The lithological interfaces close below the borehole sensors can have significant impedance contrasts. Then, local ground motions are likely influenced by elastic deformation of the soft rock layer and lithological interfaces close below borehole sensors. To simulate these effects, we moved the borehole reference point deeper, to the position of the velocity model interface below the sensor depth, indicated as 'SM reference (whole)' in Fig. 2d. Then, surface-borehole SMs also account for the elastic deformation of the soft sedimentary rock layer surrounding the borehole sensor. The resultant theoretical predictions have frequencies of amplification peaks much closer to the observed values (blue curves in Fig. 2). The fit is especially improved for fundamental resonance peaks, which justifies our approach. This implies that the elastic deformation of surrounding rocks and the effects of lithological interfaces close below the reference depth have to be considered at soft sedimentary rock sites. In addition, we tried to use a velocity gradient in the layer surrounding the borehole sensor; however, it does not improve the fit of empirical and theoretical S/B amplification curves at these particular sites. Further, green lines in Fig. 2 display the quarter-wavelength-velocity impedance contrast curves computed following the approach by [34] which are correlated but not equal to amplification. As expected, the impedance contrast has smaller amplitudes than the S/B amplification, while the frequency of the fundamental impedance peak is similar to that computed as the response of the whole 1D medium.

The fit between empirical and theoretical S/B amplification in Fig. 2 is satisfactory but not perfect. This may be caused by the presence of 2D/3D resonance effects or an imperfect reference velocity model. To tackle the latter issue, we perform the Bayesian inversion of empirical S/B amplification curves to infer a 1D medium spanning between surface and borehole sensors. The resultant PPD functions are shown in Fig. 3; these are produced by random sampling utilizing three parallel Markov chains with burn-in and production phases set to 5000 and 50,000 steps, respectively. The resultant PPD functions are in accord with reference 1D velocity models shown by blue dashed lines because the reference S-wave velocity is close to its highly probable value along the whole profile. Our inversion results are also consistent with velocity profiles inferred by [65] using horizontal-to-vertical curves of earthquake recordings. The solution of the Bayesian inversion is the whole PPD function; nevertheless, we select a representative velocity model for each site (red lines in Fig. 3). Then, these inferred velocity models are used as 1D media for the computation of adjusted theoretical surface-borehole SMs. The comparison of empirical and adjusted theoretical S/B amplification curves is shown in Fig. 4. Indeed, amplification predictions by the SM using inferred velocity models (red curves in Fig. 4) are closer to empirical data than predictions using reference

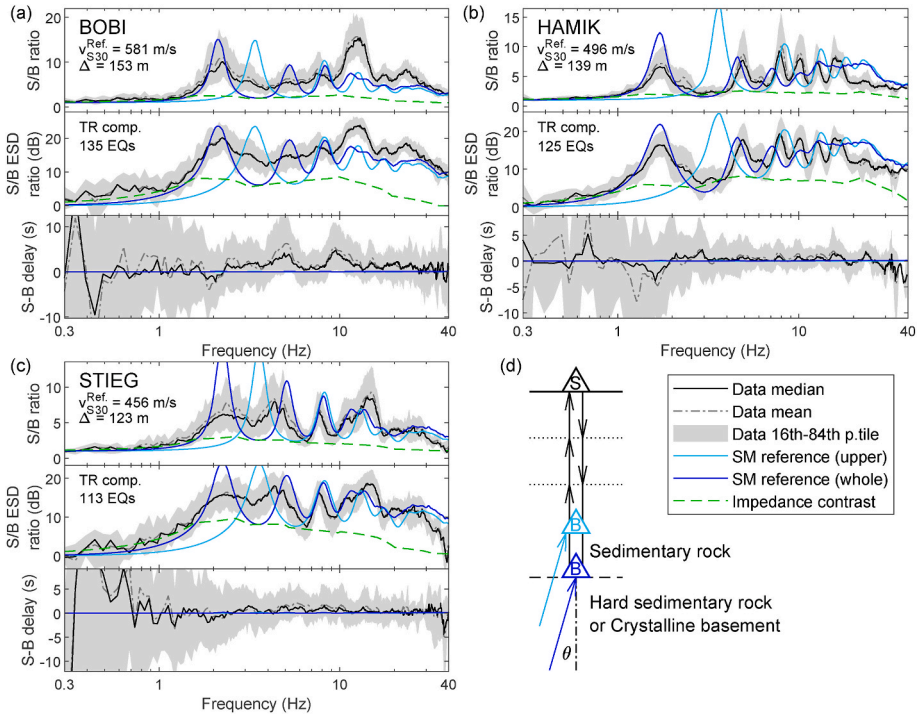


Fig. 2. Empirical surface-borehole TFs versus predictions by the SM for NAGRA sites. The empirical TFs (black curves) are computed from the transverse component of observed earthquake waveforms and complemented with 16th and 84th inter-event percentiles (gray area). Predictions by SMs are computed for the upper-structure (light-blue curves) and whole (blue curves) reference velocity models. The whole velocity models include an interface close below the depth of the borehole sensor. (a) BOBI site, (b) HAMIK site, (c) STIEG site, and (d) situation scheme.

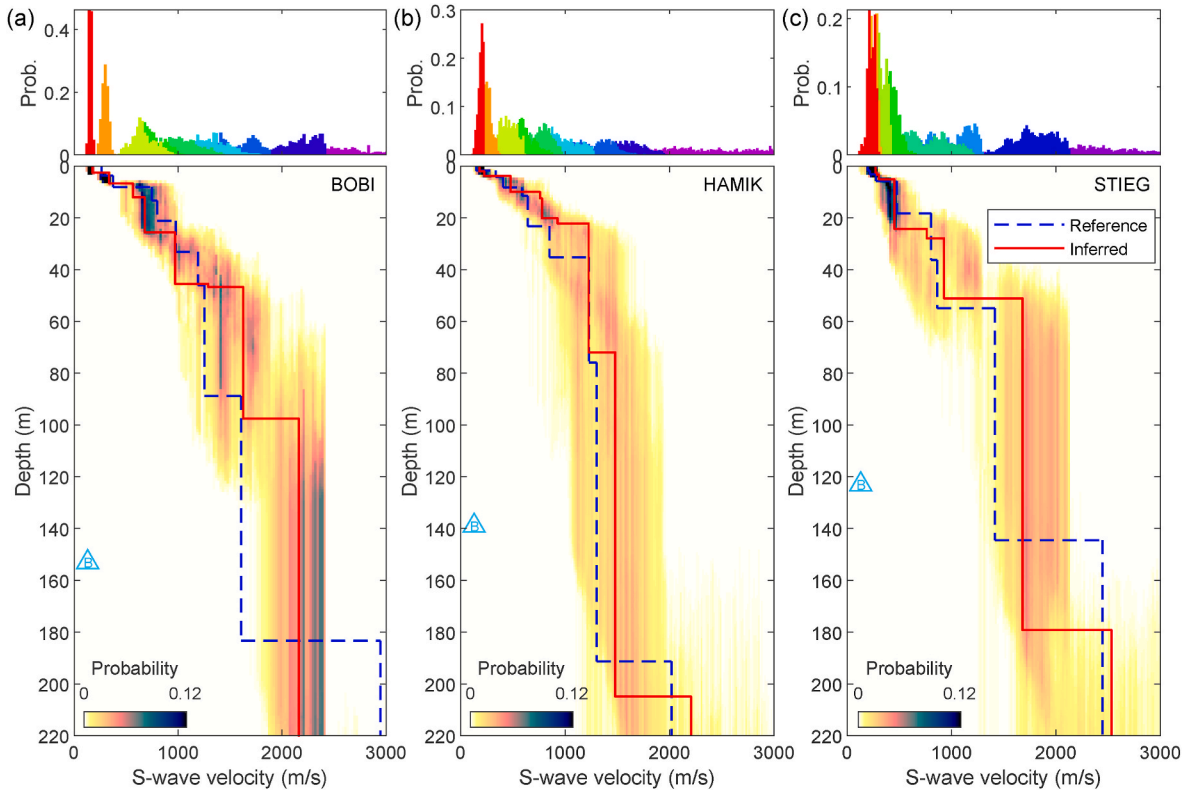


Fig. 3. Results of the Bayesian inversion of empirical surface-borehole TFs at NAGRA sites. The PPD function is shown by the color scale that expresses the probability. Blue dashed lines show reference velocity models, red lines show inferred velocity models and light blue triangles mark the depth of the borehole sensor. Histograms in the upper panels show marginal PPDs for individual layers (differentiated by color). (a) BOBI site, (b) HAMIK site, and (c) STIEG site.

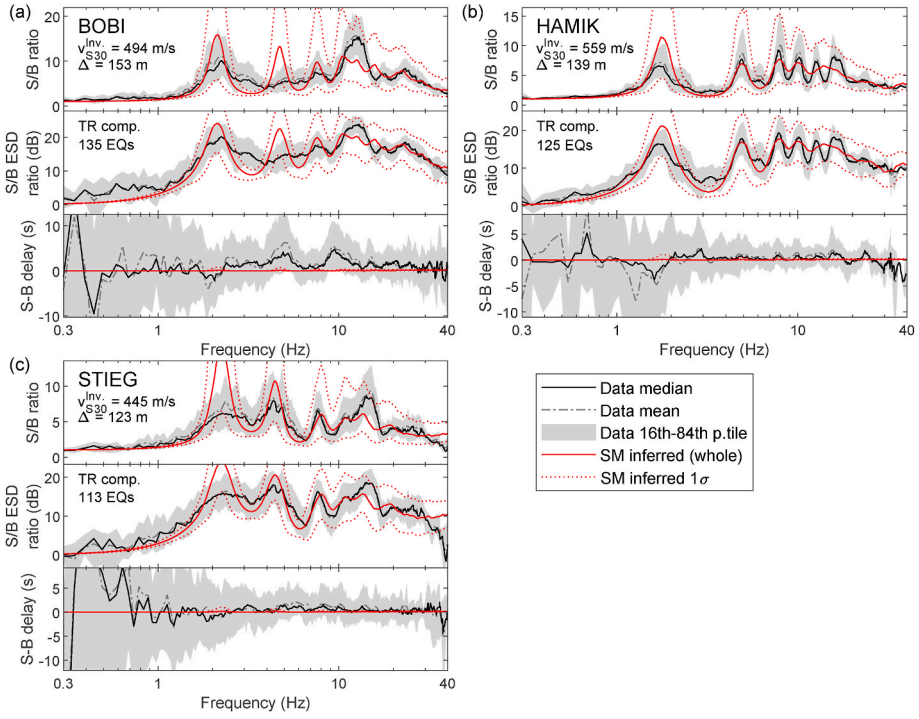


Fig. 4. Empirical surface-borehole TFs versus predictions by inferred velocity models for NAGRA sites. The empirical TFs (black curves) are computed from the transverse component of observed earthquake waveforms and complemented with 16th and 84th inter-event percentiles (gray area). Predictions by the SM (red curves) are computed for whole inferred velocity models. Velocity models include an interface close below the depth of the borehole sensor. (a) BOBI site, (b) HAMIK site, and (c) STIEG site.

velocity models (blue curves in Fig. 2), even though the inferred and reference velocity models are not strikingly different at respective sites. Next, the amplitudes at the fundamental resonance peaks are slightly overestimated. This is a common problem of modeling with 1D models and it could be caused by several factors including the stiffer structure below the borehole sensor depth, the interface irregularity, imprecisions in the velocity profile, or frequency-dependent quality factors. Nevertheless, the fit between empirical and adjusted theoretical S/B

amplification curves is good, which justifies our modification of the ground motion modeling method for the soft rock sites of the Swiss Molasse Basin.

The reference velocity models come from site characterization measurements of surface wave dispersion curves; therefore, they are compatible with field data. Hence, we can evaluate the reliability of the inferred velocity models by comparison of predicted and measured dispersion curves. The dispersion curves are computed for fundamental, 1st, and 2nd modes of Rayleigh and Love waves by using the Geopsy software [66]. As we infer S-wave velocity values only, P-wave velocities were assigned based on the v_P/v_S ratio of the reference velocity model and mass densities were assigned based on the empirical relation from [67]. The final comparison of observed data and dispersion curves of reference and inferred velocity models is shown in Fig. 5. There is a satisfactory mutual fit of dispersion curves at all sites even considering higher modes. This supports the reliability of inferred velocity models.

3.4. Results for the SVISP site

The lithology at the SVISP site (SSMNet) differs from previous ones as it is located in the Alpine valley filled with deposits (e.g., [56]). This complicates the S/B amplification function due to possible 2D/3D resonance effects and the fact that the borehole sensor is placed in unconsolidated sediments. Further, it has been noted by [56] that it is necessary to assume a positive velocity gradient to explain the empirical S/B amplification curve at this site.

The empirical surface-borehole TF is shown by black curves in the upper panels of Fig. 6. As only 15 earthquakes over a shorter monitoring period are considered at the SVISP site, this empirical curve is less robust than that at previous sites. The theoretical surface-borehole TFs from SM were computed as the response of the medium above the borehole sensor depth (the upper-structure model) and the whole 1D medium including the sedimentary layer surrounding the borehole sensor (whole model), in which the site-specific 1D reference velocity model originates from site characterization measurements [64]. Nevertheless, none of these two theoretical TFs (light-blue and blue curves in Fig. 6a) provides good fit with observed amplification peaks. Next, we implemented a gradient 1D velocity model from [56]; which accounts for the gradual change of viscoelastic parameters of unconsolidated sediments surrounding the borehole sensor. The resulting theoretical TF (purple curves in Fig. 6a) has frequencies of amplification peaks much closer to observed values. The fit is especially improved for the fundamental resonance peak, which justifies the necessity of a velocity gradient at this site. This may imply that a velocity gradient should be considered at sites with unconsolidated sediments at the depth of interest.

The fit between empirical and theoretical S/B amplifications above the fundamental frequency is not perfect at this site (purple curves in Fig. 6b). Hence, we performed the Bayesian inversion of the empirical S/B amplification to increase the accuracy of the local 1D medium. In the inversion, surface-borehole SMs were computed as a response of the 1D medium including the velocity gradient in the bottommost layer. The resultant PPD function shown in Fig. 6d is produced by three parallel Markov chains with burn-in and production phases set to 1000 and 10,000 steps, respectively. Finally, the comparison of the empirical S/B amplification curve with predictions by the inferred gradient model is shown in Fig. 6b (red curves), which shows that the inferred gradient model does not provide a strikingly improved fit to empirical data than the reference gradient model. This may indicate the influence of factors beyond 1D phenomena, i.e., the presence of 2D/3D resonance effects at the SVISP site.

4. Prediction of ground motion at depth

The design of structures for earthquake resistance requires a prediction of possible ground motions as an input. Hence, predictions of the ground motion at depth are necessary for the earthquake engineering. Following [25]; the broadband waveforms at a depth can be analytically predicted from surface recordings by using predictive TF formulated in equation (4) with the site-specific surface-borehole SM determined in Section 3. In this section, the method to predict broadband waveforms of the ground motion at depth is applied to the 2017 Urnerboden M_L4.6 (M_w4.1) earthquake and another six significant regional earthquakes with $M_L > 4$ (see Table 1).

4.1. Urnerboden earthquake

The 2017 Urnerboden M_w4.1 earthquake occurred on March 6, 2017 beneath the Urnerboden village in the Swiss canton of Uri and it is the

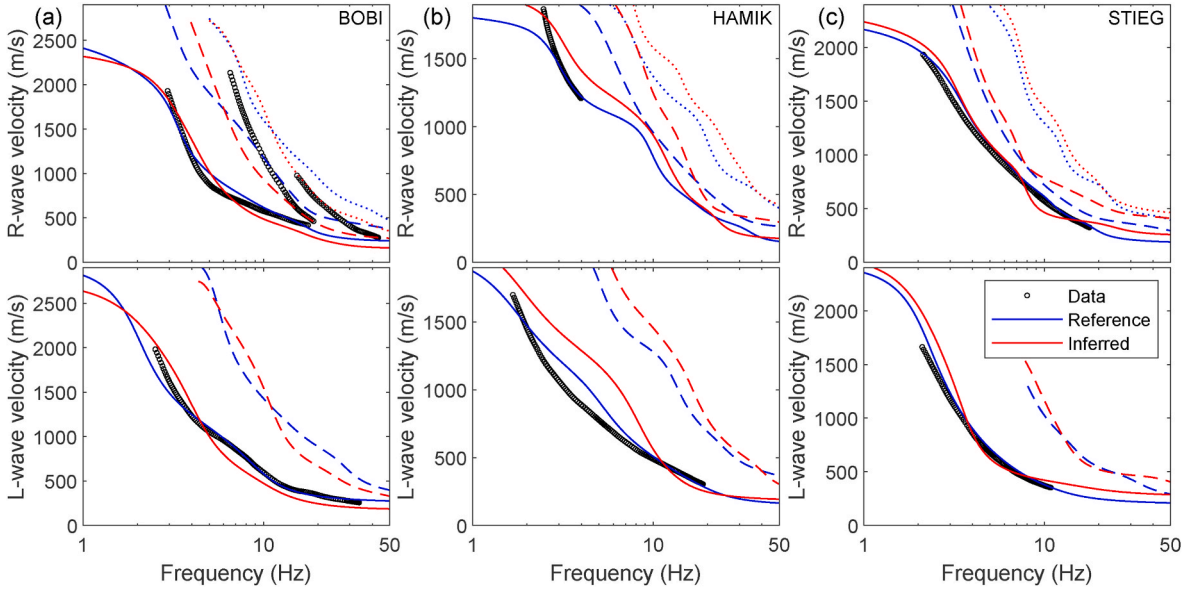


Fig. 5. Comparison of measured and predicted surface wave dispersion curves at NAGRA sites. Dispersion curves of Rayleigh (upper panels) and Love (bottom panels) waves are computed in reference velocity models (blue curves) and inferred velocity models (red curves). Reference velocity models come from site characterization measurements (black circles) while inferred models result from the Bayesian inversion shown in Fig. 3. Fundamental, 1st, and 2nd higher modes of surface waves are shown by solid, dashed, and dotted lines, respectively. (a) BOBI site, (b) HAMIK site, and (c) STIEG site.

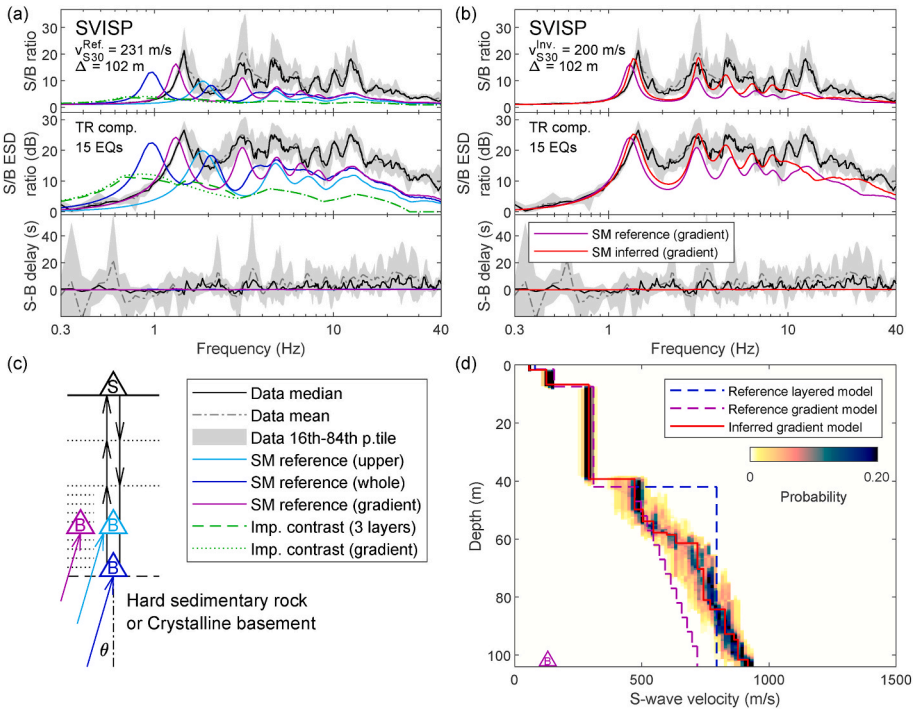


Fig. 6. Empirical surface-borehole TFs versus theoretical predictions at the SVISP site. The empirical TFs (black curves in upper panels) are computed from the transverse component of observed earthquake waveforms and complemented with 16th and 84th inter-event percentiles (gray area). In (a), predictions by SMs are computed for the upper-structure (light-blue curves), whole (blue curves), and gradient (purple curves) reference velocity models. In (b), predictions by the SM are computed for the reference (purple curves) and inferred (red curves) gradient velocity models. (c) is the situation scheme, and (d) shows the result of the Bayesian inversion of the empirical surface-borehole TF.

strongest event in the waveform database used in this study [35]. Here, predicted waveforms at depth are compared with observed ones in boreholes using both temporal and frequency domains.

In Figs. 7 and 8, we show predictions of the ground motion at depth from surface recordings at the BOBI and HAMIK sites, respectively. First, in Fig. 7a, we show the transverse component of the surface motion observed at the BOBI site which is located 84 km away from the epicenter. This waveform has distinctive Pg, PmP, Sg, and SmS seismic phases. Values of PGA, PGV, and I_A measured on the ground surface are 1.25 cm/s^2, 0.051 cm/s, and 0.0019 cm/s, respectively. Note that the envelope delay has values around 30 s after the event origin, which can be associated with the S-wave phase arrival. In Fig. 7b, we compare the theoretical prediction of the ground motion at depth (red curves) with the transverse component observed in the borehole (black curves). The prediction is very close to the observed values within the frequency range of 0.3–40 Hz. The predicted and observed PGA at depth have

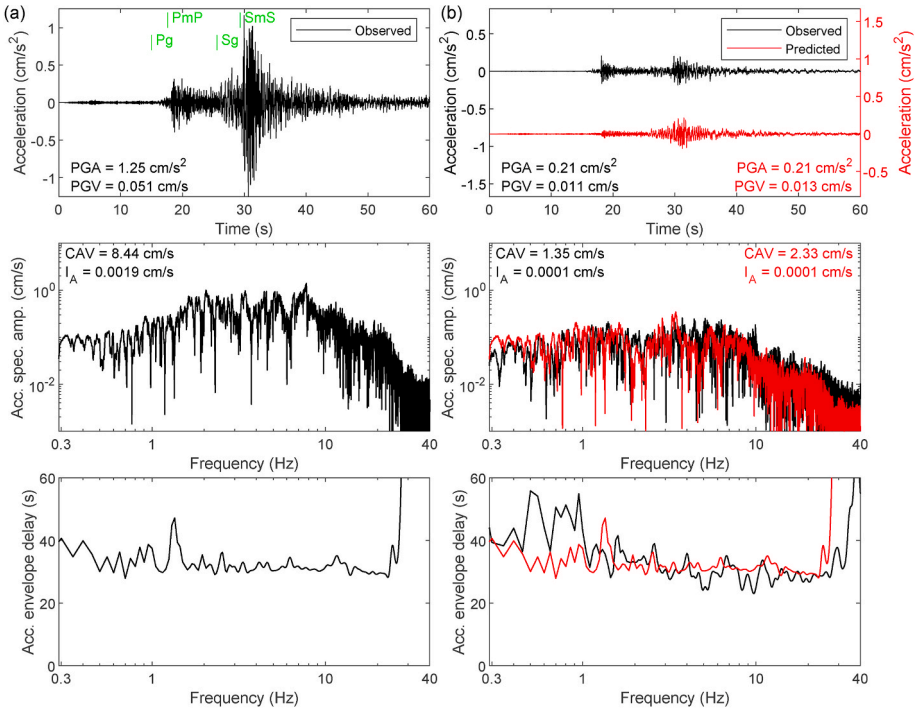


Fig. 7. Full-waveform prediction of ground motion at depth from surface recordings of the M_w4.1 Urnerboden earthquake. It shows empirical data (black curves) and the theoretical prediction (red curves) at the BOBI site of the NAGRA network (epicentral distance 84 km). Acceleration waveforms, amplitude spectra, and envelope delays of the transverse horizontal component are shown (a) on the ground surface, and (b) in the borehole at 153 m depth.

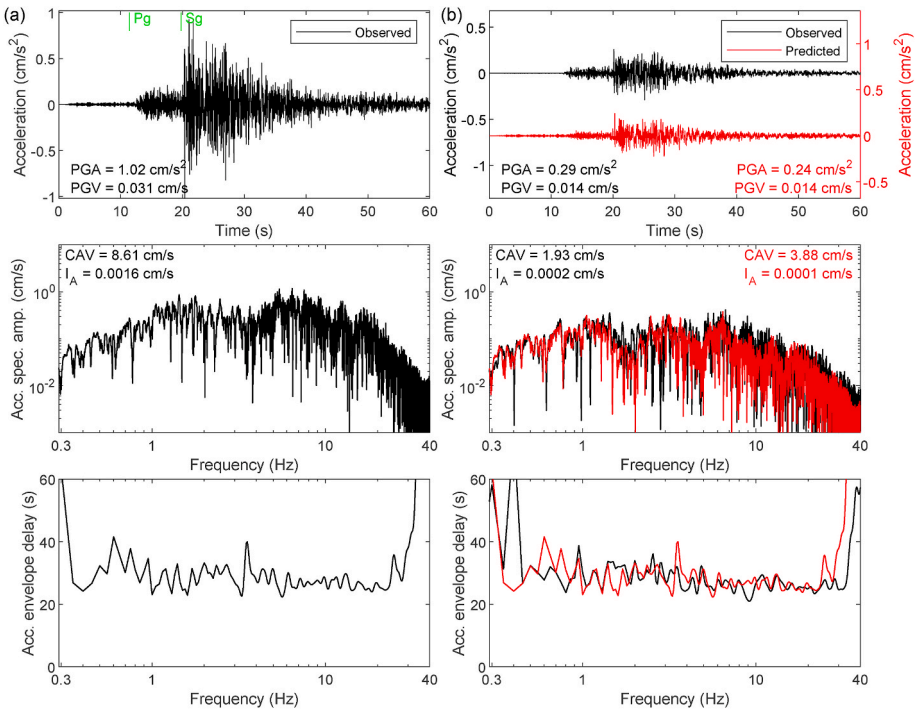


Fig. 8. Full-waveform prediction of ground motion at depth from surface recordings of the M_w4.1 Urnerboden earthquake. It shows empirical data (black curves) and the theoretical prediction (red curves) at the HAMIK site of the NAGRA network (epicentral distance 62 km). Acceleration waveforms, amplitude spectra, and envelope delays of the transverse horizontal component are shown (a) on the ground surface, and (b) in the borehole at 139 m depth.

exactly the same value of 0.21 cm/s^2; predicted and observed PGV have values of 0.013 and 0.011 cm/s, respectively; predicted and observed I_A at depth have the same value of 0.0001 cm/s. Note that both Sg and SmS seismic phases are well predicted by our method because they are horizontally polarized S-waves at the onset at depth regardless of the path from the source.

Second, the HAMIK site is located at a distance of 62 km from the epicenter, and the ground motion prediction at depth is shown in Fig. 8. At this site, the waveform has distinctive Pg and Sg seismic phases only. The theoretical prediction of the ground motion at depth (red curves) is very close to values observed in the borehole (black curves) within a broad frequency range as well, note especially well-fitted details of Fourier's spectra at about 2 and 5 Hz in Fig. 8b. Expressed by numbers, the predicted and observed PGA at depth have values of 0.24 and 0.29 cm/s^2, respectively, while predicted and observed PGV have exactly the same value of 0.014 cm/s at the HAMIK site. These two examples

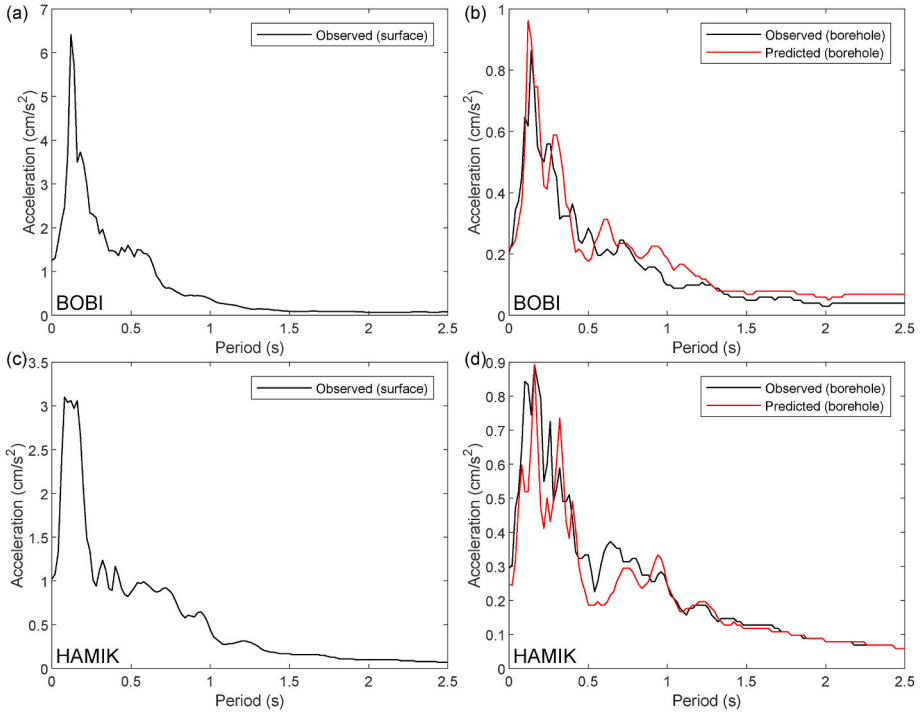


Fig. 9. Acceleration response spectra computed from observed and predicted waveforms of the M_w4.1 Urnerboden earthquake. There are elastic response spectra for observed waveforms (black curves) and the theoretical prediction (red curves) at BOBI and HAMIK sites (top and bottom panels, respectively). Panels (a) and (c) show response spectra on the ground surface while panels (b) and (d) at the depth of 153 and 139 m, respectively. This figure is extended by the goodness-of-fit statistics in Appendix C.

demonstrate the applicability of the method to predict full broadband waveforms at depth at Swiss soft rock sites.

Finally, we computed acceleration response spectra on the ground surface and at depth. The response spectra are computed by the Newmark time-integration method using the program PRISM which is intended for the seismic response analysis of single-degree-of-freedom systems [68]. The response spectra are computed for a viscous damping value of 0.05 and they are shown for the BOBI and HAMIK sites in Fig. 9. As expected, response spectra have larger acceleration values on the ground surface than at depth. A less intuitive yet important result is that the shape of response spectra differs between surface and boreholes, which implies that response spectra scaling by simple multiplication would not be the correct procedure. On the other hand, response spectra at depth computed from observed and predicted waveforms are reasonably similar to each other in terms of both values and shape. The rigorous goodness-of-fit of observed and predicted response spectra at depth by means of coherence and cross-correlation is shown in Appendix C. This validates our prediction method for engineering applications.

4.2. Statistics from significant regional earthquakes

To statistically evaluate the comparison of predicted and observed ground motions at depth, we repeated the analysis for another six significant regional earthquakes from Table 1. We deconvolved broadband seismic waveforms at depth from surface recordings at all six borehole sites considered in this paper. Unfortunately, not all the borehole stations were in operation when these earthquakes occurred or the epicentral distance was too large; hence, the resultant set consists of 22 earthquake-station pairs. Analogically to the 2017 Urnerboden earthquake, borehole waveforms were predicted by using the predictive TF formulated in equation (4) utilizing the site-specific surface-borehole SMs determined in Section 3. Then, we evaluated the PGA, PGV, Arias intensity, and maximum value of acceleration response spectra from observed and predicted broadband waveforms at depth.

The statistical comparison of values determined from observed and predicted waveforms at depth is shown in Fig. 10. The comparison can be performed jointly for various earthquakes and sites as we compare the ratio between observed and predicted values. The optimal ratio is 1:1, in which predicted values exactly match observed ones (black dashed lines). Values above the dashed line are overpredicted and *vice versa*. The quantitative comparison is performed using the logarithmic Nash-Sutcliffe model efficiency coefficient E [69]. It indicates how well the observed versus predicted data fits the 1:1 line ($E = 1$ for the perfect fit), and it is calculated from logarithmic values in order to have balanced sensitivity in a wide range. In all monitored characteristics of the ground motion at depth, values for various earthquakes and sites are spread closely to the 1:1 ratio, and the coefficient E has high values (note a very good performance with $E > 0.85$ for PGA and Arias intensity). This is an encouraging result, which demonstrates the good performance of our method to predict ground motions at depth from surface recordings.

5. Modeling of broadband waveforms

The prediction of the ground motion at depth from surface recordings (i.e., Section 4) is limited to past earthquakes. However, in regions characterized by moderate seismicity, we lack waveform recordings of strong ground motions. For the local seismic hazard assessment, we need to perform predictions of potentially damaging ground motions that can occur in the future. For such a purpose, we use synthetic broadband waveforms, modeled by the SCEC Broadband Platform on the ground surface at the site of our interest. First, we perform a validation test to compare simulated and observed surface waveforms for the 2017 Urnerboden M_w4.1 earthquake. The purpose of this test is to evaluate the capability of the deployed method to simulate broadband waveforms in the Swiss Molasse Basin. Second, for demonstration purposes, we model synthetic broadband waveforms for a scenario earthquake that may occur in 9975 years return period at the BOBI site (test site). The results from the scenario simulation are subsequently used for the prediction of ground motion and the respective response spectrum at depth.

5.1. Validation by the simulation of urnerboden earthquake

First, we use the BBP to model synthetic waveforms for the 2017 Urnerboden M_w4.1 earthquake. This earthquake was a strike-slip event with a shallow focal depth of about 4 km and its source model was inferred by previous studies with high accuracy. For the broadband

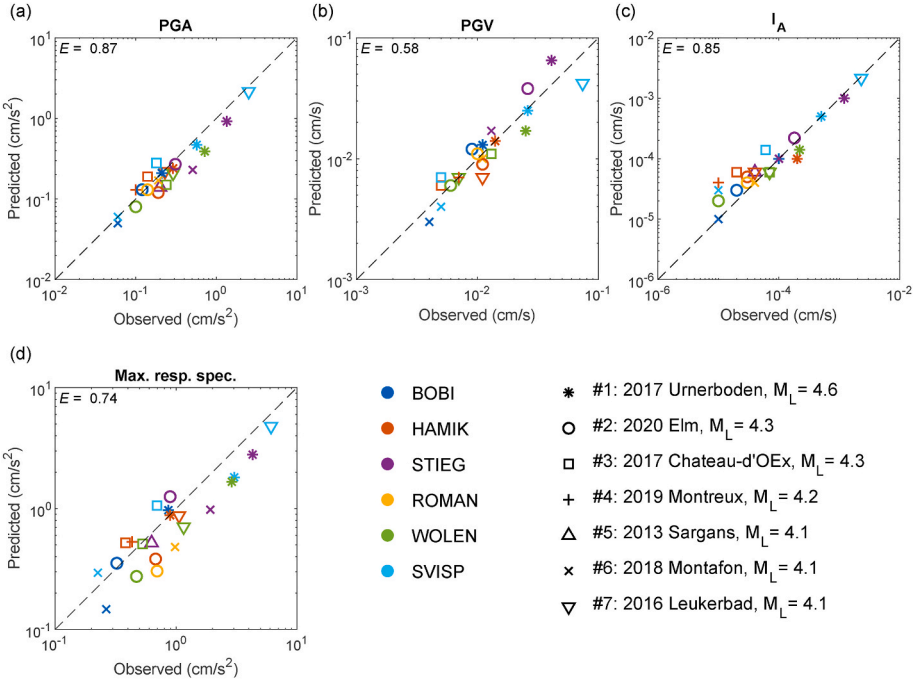


Fig. 10. Statistical comparison of observed and predicted ground motions at depth for significant regional earthquakes in Switzerland. Ground motions at depth are predicted for six borehole sites (distinguished by color) and earthquakes from Table 1 (distinguished by marker symbol). Panels (a), (b), (c), and (d) show the comparison of PGA, PGV, Arias intensity, and maximum value of acceleration response spectra at depth, respectively. E is the Nash-Sutcliffe model efficiency coefficient calculated with logarithmic values.

modeling purpose, we set source parameters exactly as inferred by [35]; which are summarized in Table 2. We would like to emphasize that we performed no tuning of source parameters; hence, the comparison of simulated and observed waveforms objectively evaluates the modeling method. The hybrid modeling method by [51] first generates a random distribution of the heterogeneous slip on the fault plane and then computes synthetic waveforms.

The resultant synthetic and observed transverse horizontal components of the surface ground motion are shown in Fig. 11. The comparison is shown in the temporal and Fourier domains at the HAMIK site which is located at an epicentral distance of 62 km (distinctive Pg and Sg seismic phases). The similarity between synthetic and observed waveforms is satisfactory in terms of both amplitudes and envelopes in the initial part of the waveforms. In the temporal domain, the timing of phase arrivals is accurate and the only dissimilarity is a shorter duration of the synthetic waveform, which may be due to underestimated wave scattering and reverberations in the BBP tool. In the Fourier domain, spectral amplitudes of the synthetic waveform are slightly underestimated, which is probably due to the shorter waveform duration and simplistic modeling of the site term through v_{S30} adjustments. Nevertheless, it may be improved in future studies. Finally, values of PGA, PGV, and I_A obtained from the synthetic waveform compare well to the observed ones. In particular, modeled PGA and PGV are equal to 1.04 cm/s^2 and 0.036 cm/s, which are very close to the observed values of 1.02 cm/s^2 and 0.031 cm/s, respectively. The modeled I_A of 0.0011 cm/s is lower than the observed value of 0.0016 cm/s due to the shorter duration of the synthetic waveform.

Altogether, the utilized broadband waveform modeling with the regional 1D velocity model performs well and satisfactorily models seismic waveforms observed on the ground surface in the Swiss Molasse Basin. Naturally, the broadband waveform modeling method can be improved in the future, but that is not the focus of this study. Once again, we performed no tuning of the source model parameters; hence, this validation of the modeling method is objective.

5.2. Scenario earthquake modeling

Next, we perform an earthquake scenario simulation to demonstrate the potential of the method to predict ground motions at depth caused by future earthquakes in Switzerland. We would like to emphasize that this analysis is just for demonstration purposes and it is not intended to assess the seismic hazard at depth for a specific underground repository. The selected earthquake scenario is the dominant event from disaggregation of the Swiss seismic hazard model SUIhaz15 [36] for the return period of 9975 years at the BOBI site. The used disaggregation by [37] assesses the relative contribution to the exceedance of PGA from various magnitude-distance earthquake scenarios. Then, the dominant event is the earthquake scenario with the largest contribution at the given location. In the case of the BOBI site, the dominant event is an M_w5.8 earthquake in the 5 km Joyner-Boore distance (i.e., the closest horizontal distance from the site to the vertical projection of the fault plane onto the Earth's surface). According to the seismic hazard model SUIhaz15 for the 9975 years return period, the PGA is expected to exceed 200 cm/s^2 at the BOBI site (measured on the Swiss reference rock with v_{S30} of 1106 m/s; [70]. For the broadband waveform modeling, the fault geometry and depth are defined by the preferred faulting style within the respective seismotectonic zone following [36] which is summarized in Table 3. The fault-plane depth is deeper than in the case of the Urnerboden earthquake because observed earthquake hypocenters are located deeper in the Swiss Molasse Basin than in the Alpine areas. The random distribution of the heterogeneous slip on the fault is generated following [51] with average and maximum slip values of 30 and 102 cm, respectively.

Table 2
Urnerboden M_w4.1 earthquake source model used in broadband waveform modeling.

M_w	Strike/Dip/Rake (deg)	Fault size (km)	Fault depth (km)	Mean slip (cm)
4.1	348/86/5	0.6 × 0.6	3.7–4.3	18

The resultant synthetic broadband waveform (i.e., the dominant horizontal component of ground motion) modeled on the ground surface is shown in Fig. 12a and Fig. D1. Due to the small epicentral distance, Pg and Sg seismic phases arrive in quick succession followed by the later SmS phase (i.e., S-wave reflected by the Moho discontinuity at 29.8 km depth). The Fourier spectrum has a broadband character and the response spectrum computed by the Newmark time-integration method resembles those from engineering design codes. Expressed by numbers, the dominant horizontal component of the ground motion simulated on the surface has values of PGA, PGV, and I_A equal to 310.9 cm/s^2, 18.04 cm/s, and 49.48 cm/s, respectively. Indeed, such values are expectable for the given magnitude, distance, and site conditions (v_{S30} equal to 581 m/s at the BOBI site). Note that the PGA of the modeled waveform is larger than the expected value from the seismic hazard model SUIhaz15, this is reasonable because the site-specific v_{S30} value is smaller than that of the Swiss reference rock profile. Next, the prediction of the ground motion at depth for this earthquake scenario is shown in Fig. 12b and Fig. D2. The prediction makes use of the surface-borehole SM determined at the BOBI site in Section 3.3 and the predictive TF formulated by equation (4). The broadband waveform predicted at the 153 m depth looks reliable and yields PGA, PGV, and I_A values of 64.8 cm/s^2, 7.53 cm/s, and 2.839 cm/s respectively.

Finally, we computed the response spectrum from the broadband waveform predicted at depth. The response spectrum at depth has smaller amplitudes and a different shape compared to the one on the ground surface. An interesting feature is a peak at the period of about 0.3 s, which can be associated with the 3.3 Hz peak in the Fourier spectrum. This feature may be site-specific due to local stratigraphy (this peak is also noticeable in the case of the Urnerboden earthquake in Fig. 9b) and should be investigated at the particular site of the planned deep geological disposal. Such an analysis is important as the spectral peak can cause potentially dangerous resonances of structure parts that have the same nature frequency. To summarize, we demonstrated that the proposed method can be used for the prediction of the ground motions at depth caused by future earthquakes and it may be used for the site-specific seismic hazard at depth for long return periods.

6. Conclusions

In this paper, we characterized high-frequency ground motion at depth in soft sedimentary rocks of the Swiss Molasse Basin and used it to predict broadband waveforms at depth for past and future earthquakes.

First, we determined empirical S/B amplification functions at six borehole sites equipped with surface and borehole sensors at depths of 98–153 m, and compare them with theoretical amplification functions computed by using the stochastic model introduced by [25]. The empirical and theoretical S/B amplification curves have a high level of similarity, which implies the good performance of the implemented site-response modeling method.

Further, our results imply that the mechanical properties of rocks at the depth of interest have a significant influence on the local S/B amplification function. We draw the following conclusions: i) in the case of an underground site located in hard rock, the surface-borehole TF can be computed as the response of the medium only above the underground site depth, ii) if the underground site is located within soft sedimentary rocks, the elastic deformation of the surrounding soft rock layer and the effect of lithological interfaces close below should be considered, and iii) in the case of an underground site located in unconsolidated sediments, one should evaluate the effect of the velocity gradient on the surface-borehole TF.

Next, we performed an analytical prediction of ground motion at

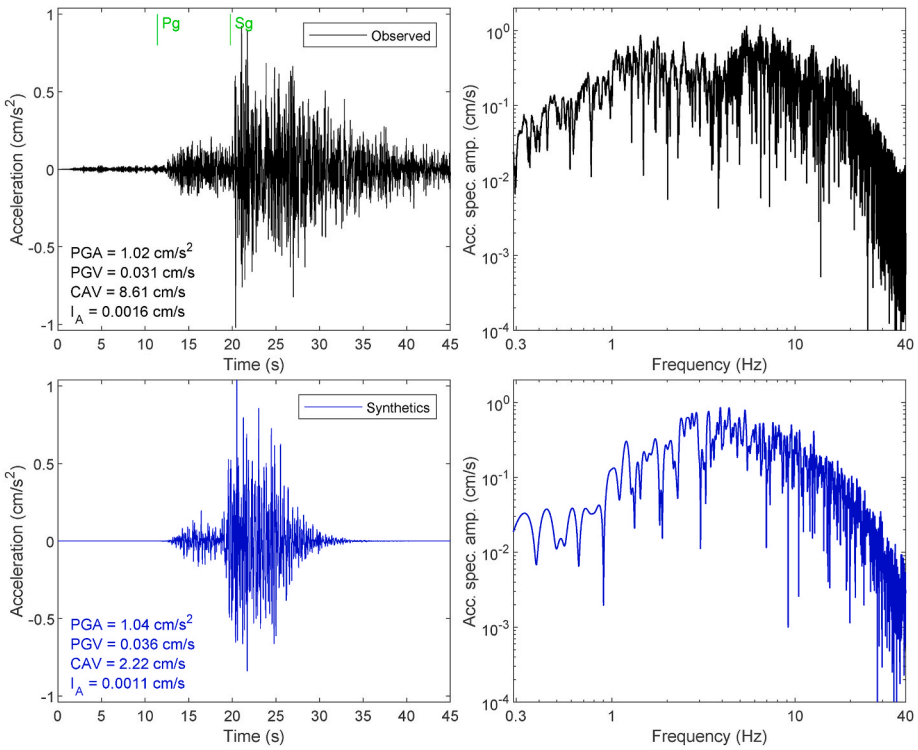


Fig. 11. Validation of the broadband waveform modeling by using the M_w4.1 Urnerboden earthquake. The waveform observed on the ground surface at the HAMIK site is shown by the black curve (upper panels). The synthetic waveform modeled by the SCEC Broadband Platform is shown by the blue curve (bottom panels). The displayed waveforms are transverse horizontal components of the ground acceleration.

Table 3
Scenario M_w5.8 earthquake source model used in broadband waveform modeling.

M_w	Strike/Dip/Rake (deg)	Fault size (km)	Fault depth (km)	Mean/Max. slip (cm)
5.8	300/87/−176	8 × 8	7–15	30/102

depth from surface recordings of the M_w4.1 Urnerboden earthquake and another six significant regional earthquakes. This analysis is very valuable as it is rarely performed and statistically evaluated. The comparison of predicted and observed waveforms shows a high level of similarity in the whole frequency range of 0.3–40 Hz (Figs. 7 and 8). Predicted values of PGA and PGV at depth are close to values measured on a horizontal component in boreholes, and response spectra at depth could be satisfactorily predicted as well (Fig. 9). On top of that, the statistical comparison of predicted and observed characteristics of the ground motion at depth of significant earthquakes in Fig. 10 implies a very good performance of our method to predict ground motions at depth from surface recordings.

Finally, we tackled the issue of predicting the ground motion at depth caused by future potentially damaging earthquakes. To do so, we modeled synthetic broadband waveforms for the M_w5.8 scenario earthquake in 5 km Joyner-Boore distance (an event from the site-specific disaggregation of seismic hazard for 9975 years return period), and we predicted associated broadband waveforms at depth (Fig. 12). This analysis revealed that the PGA at depth can be as large as 64 cm/s^2 and the maximum amplitude of the response spectrum at depth can exceed 0.25 *g* at the test site within the 9975 years return period. Such a ground motion may cause damage to sensitive parts of the underground structure if neglected during the construction design. By this example, we demonstrated that the method can be used as a basis for the site-specific seismic hazard assessment at depth.

Availability of data and materials

The waveform data underlying this article can be obtained following instructions on the webpage http://www.seismo.ethz.ch/en/research-and-teaching/products-software/waveform-data/, [73]; DOI: 10.12686/SED/NETWORKS/CH). The station site characterization data can be accessed at http://stations.seismo.ethz.ch/, [64]; DOI: 10.12686/SED-STATIONCHARACTERIZATIONDB). Both websites were last accessed on April 23, 2023.

Code availability

Plots were made using Matlab software version 2021a [74] and the Generic Mapping Tools version 6.0.0 [75]. The surface-borehole SMs were computed by the original software from [25]. The dispersion curves of surface waves were computed by using the Geopsy software version 3.3.6 [66]. Response spectra were computed by the PRISM software version 2.0.1 [68]. Synthetic surface seismograms were modeled using the SCEC Broadband Platform version 19.4.0 [48]. Green's functions were modeled by using the Fk software version 3.2 [52] with an additional Bailey output format.

Ethics approval and consent to participate

Not applicable.

Consent for publication

The authors declare that they have permission to publish the research findings included in this paper.

Funding

This project is supported by the Swiss Federal Nuclear Safety

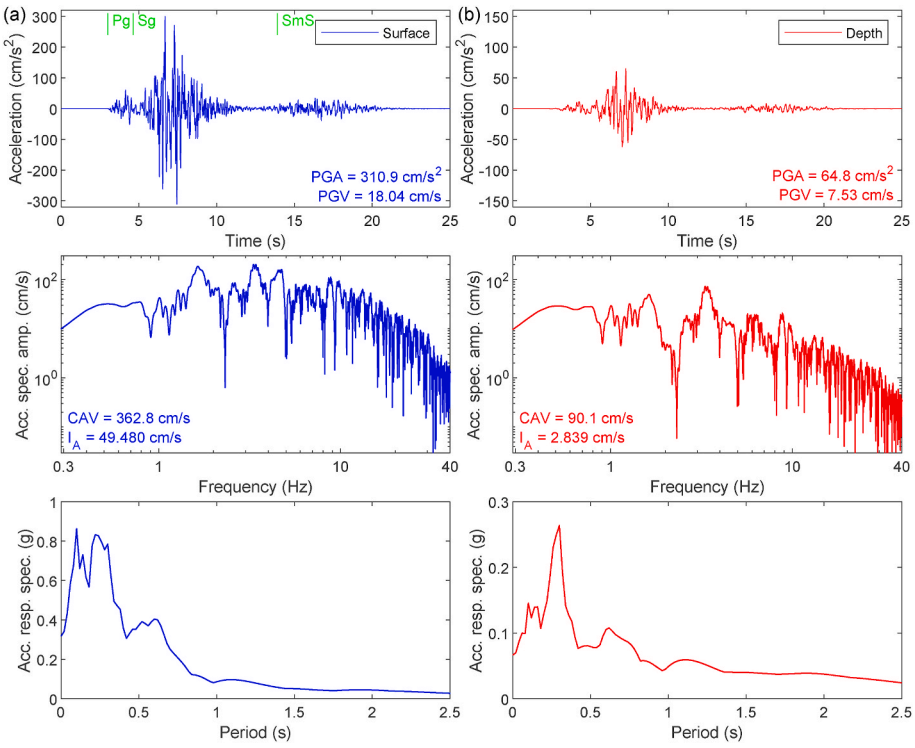


Fig. 12. Full-waveform prediction of ground motion at depth for the M_w5.8 earthquake scenario. Acceleration waveforms, Fourier spectra, and elastic response spectra of the dominant horizontal component are shown for (a) synthetic broadband waveform modeled on the ground surface at the BOBI site (Joyner-Boore distance 5 km from the assumed fault plane), and (b) borehole waveform predicted at 153 m depth from surface synthetics. This figure is extended by additional plots in Appendix D.

Inspectorate (ENSI) through contract number CTR00830.

Author contributions

Miroslav Hallo: Conceptualization, Methodology, Software, Validation, Formal analysis, Visualization, Resources, Writing - Original Draf; **Afifa Imtiaz**: Investigation, Resources, Writing - Review & Editing; **Maria Koroni**: Formal analysis, Writing - Review & Editing; **Vincent Perron**: Data Curation, Writing - Review & Editing; **Donat Fäh**: Conceptualization, Resources, Supervision, Writing - Review & Editing.

Declaration of competing interest

The authors declare that they have no known competing financial interests or personal relationships that could have appeared to influence the work reported in this paper.

Acknowledgements

Miroslav Hallo and Maria Koroni were supported through a contract with the Swiss Federal Nuclear Safety Inspectorate (ENSI), contract number: CTR00830. Afifa Imtiaz was supported by the canton of Basel-Stadt through the project 'Earthquake Risk Model Basel-Stadt'. The authors acknowledge the National Cooperative for the Disposal of Radioactive Waste (NAGRA), the Swiss Digital Seismic Network (SDSNet), and the Swiss Strong Motion Network (SSMNet) for financing and operating borehole-monitoring stations used in this study. The authors especially thank Giulia Sgattoni for the discussion and help with Green's functions modeling. The authors are grateful to Editor-in-Chief Hesham El Naggar and two anonymous reviewers, who helped to improve this paper. This work was created by humans without any help from artificial intelligence.

Appendix A. Regional velocity model

The hybrid waveform modeling method of the BBP (Section 2.5) requires a velocity model that is used for the computation of Green's functions. For this purpose, we constructed a regional 1D velocity model of the Swiss Molasse Basin from the Mittelland model [71]. Our velocity model has a reduced number of layers together with preserved vertical travel times of the Mittelland model. Depths of the main structural interfaces with large velocity contrast are preserved as well. Additionally, four uppermost near-surface layers were added from site characterization at NAGRA sites. The quality factors for S-waves were approximated to be one-tenth of the S-wave velocity in m/s [44]. Moreover, we verified that values of these theoretical quality factors are consistent with empirical values inferred at the 4 and 9 km depth by the crustal tomography [72]. Our regional 1D velocity model consists of 16 homogeneous layers on half-space and it is shown in Fig. A1 and Table A1. The model has v_{S30} of 590 m/s and the Moho is located at 29.8 km depth.

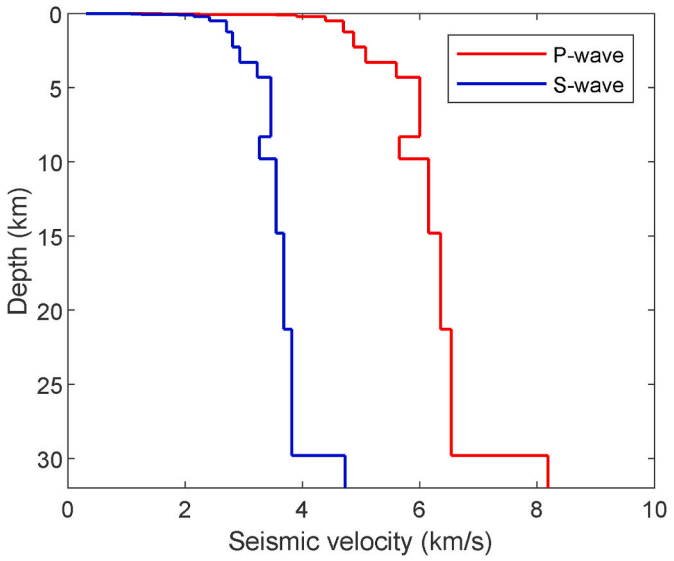


Fig. A1. Regional 1D velocity model used for the broadband waveform modeling.

Table A1
Regional 1D velocity model used for the broadband waveform modeling.

Depth (km)	P-wave velocity (km/s)	S-wave velocity (km/s)	P-wave quality factor	S-wave quality factor
0.000	0.521	0.314	39	31
0.008	1.191	0.778	90	78
0.021	1.601	1.077	120	108
0.046	2.245	1.252	169	125
0.071	3.549	1.886	248	189
0.10	3.897	2.144	273	214
0.20	4.394	2.413	308	241
0.50	4.700	2.709	329	271
1.25	4.874	2.810	341	281
2.25	5.078	2.928	355	293
3.30	5.600	3.230	392	323
4.30	6.000	3.460	420	346
8.30	5.651	3.262	396	326
9.80	6.150	3.550	431	355
14.80	6.354	3.676	445	368
21.30	6.539	3.819	458	382
29.80	8.183	4.729	573	473

Appendix B. Characterization of ROMAN and WOLEN sites

In Section 3, we compare empirical surface-borehole TFs with theoretical predictions by the surface-borehole SM at Swiss borehole sites. The SDSNet borehole sites ROMAN and WOLEN are of secondary importance for this paper's purpose; hence, the detailed characterization is present here instead of in the main text. There are no available site characterization measurements at these sites; hence, near-surface S-wave velocity profiles are not clear. From borehole stratigraphic profiles, it seems that borehole sensors are placed in soft sedimentary rocks as in the case of NAGRA sites.

The empirical surface-borehole TFs are shown by black curves in the upper panels of Fig. B1. It is not possible to directly compare empirical and theoretical S/B amplification curves at these sites, because the computation of the surface-borehole SM requires a reference S-wave velocity model. Hence, we first perform the Bayesian inversion of empirical S/B amplification curves to obtain a 1D medium spanning between surface and borehole sensors. Similar to NAGRA sites, surface-borehole SMs are assumed to be a response of the whole medium including the elastic deformation of the assumed soft sedimentary rock layer at the borehole sensor depth. The resultant PPD functions are shown in the bottom panels of Fig. B1 (burn-in and production phases set to 5000 and 50,000 steps, respectively). The empirical and inferred theoretical S/B amplification curves match each other well at both of these sites (red curves in the upper panels of Fig. B1).

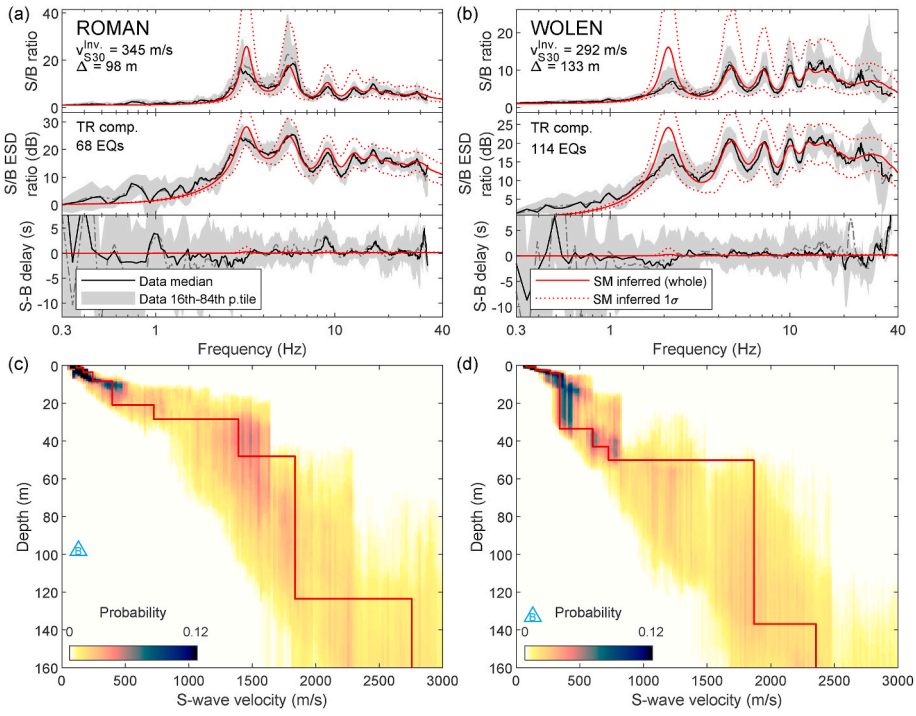


Fig. B1. Empirical surface-borehole TFs versus predictions by inferred velocity models for SDSNet sites. Panels (a) and (b) show surface-borehole TFs, while (c) and (d) show the inference of velocity models at the ROMAN and WOLEN sites, respectively. The empirical TFs (black curves) are computed from the transverse component of observed earthquake waveforms and complemented with 16th and 84th inter-event percentiles (gray area). Predictions by the SM (red curves in upper panels) are computed for whole inferred velocity models (red lines in bottom panels).

From the geological perspective, the inferred simplified stratigraphy indicates unconsolidated sediment thickness of 10–20 m at ROMAN and 50–75 m at the WOLEN site, which seems coherent with the depth of the first major contrast observed in the inferred velocity profiles. At the ROMAN site, the bottom depth of the UFM layer below could exceed 200 m, rendering the geophysical bedrock at a deeper position. As UFM consists of relatively younger and softer fluvial deposits, it is expected to show a weaker and gradient-like contrast with the overlying unconsolidated sediments and a stronger contrast with the underlying bedrock. At the WOLEN site, the LFM layer consisting of more consolidated sandstones and marls is expected to show a larger impedance contrast at the interface with the overlying unconsolidated sediments, which is reasonably reflected in the inferred velocity profile at this site.

Appendix C. Similarity of response spectra at depth

In Section 4.1, we evaluate acceleration response spectra at depth from observed and predicted borehole waveforms of the M_w4.1 Urnerboden earthquake (Fig. 9). The observed and predicted response spectra at depth seem to be very similar at both BOBI and HAMIK sites; nevertheless, we provide rigorous goodness-of-fit statistics here.

First, we evaluate the coherence between observed and predicted response spectra at depth. The coherence $C_{OP}(f)$ is defined as

$$C_{OP}(f) = \frac{|G_{OP}(f)|^2}{G_{OO}(f)\, G_{PP}(f)}, \tag{C.1}$$

in which $G_{OP}(f)$ is the cross-spectral density between the observed and predicted response spectra, and $G_{OO}(f)$ and $G_{PP}(f)$ are auto spectral densities of observed and predicted response spectra, respectively. All the spectral density functions $G(f)$ are smoothed by the Gaussian filter of a width of 11 samples. The coherence can have values between 0 and 1. If $C_{OP}(f) = 1$, it means that the response spectra are perfectly linearly related. The coherence was evaluated for both BOBI and HAMIK sites and it is shown in the left panels of Fig. C1. It has very high values (>0.9) and it is close to unity for periods longer than 1 s. It means that the observed and predicted response spectra at depth are highly correlated.

Second, we evaluate the normalized cross-correlation between observed and predicted response spectra at depth (right panels in Fig. C1). The cross-correlation functions are precisely centered at zero lag and have cross-correlation coefficients larger than 0.96. It means that the observed and predicted response spectra at depth are highly correlated and there is no mutual frequency shift.

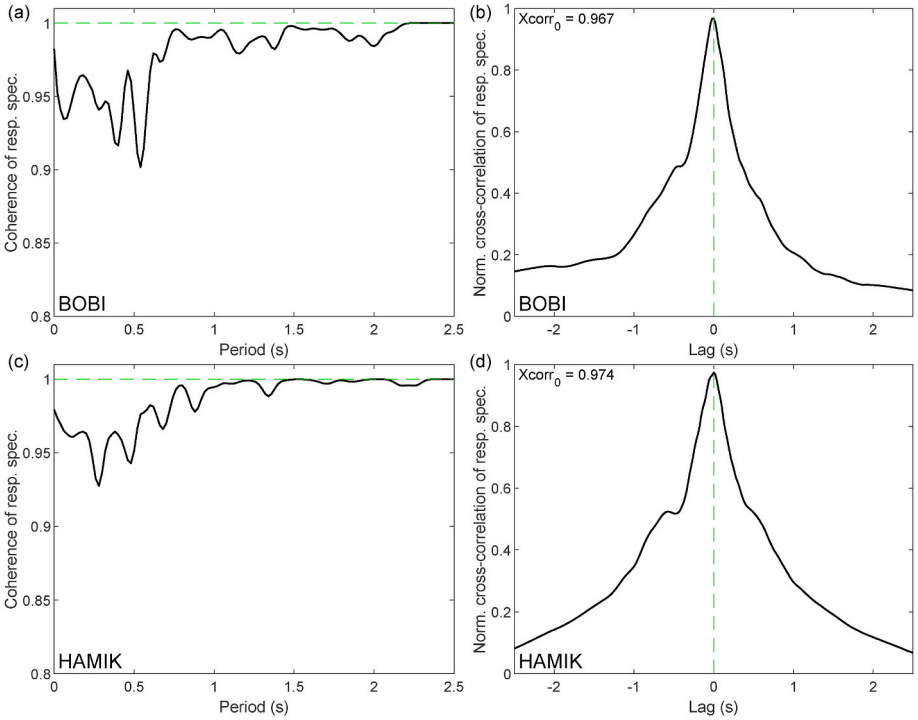


Fig. C1. Goodness-of-fit statistics for acceleration response spectra at depth computed from observed and predicted waveforms of the M_w4.1 Urnerboden earthquake. The goodness-of-fit is expressed by coherence (left panels) and normalized cross-correlation (right panels) at BOBI and HAMIK sites (top and bottom panels, respectively). In coherence plots, the green dashed lines denote unity, where observed and predicted response spectra are completely correlated. In cross-correlation plots, the green dashed lines denote zero lag between observed and predicted response spectra. This figure extends Fig. 9.

Appendix D. Scenario earthquake waveforms

In Section 5.2, we model synthetic broadband waveforms for the M_w5.8 earthquake scenario in the 5 km Joyner-Boore distance by the method described in detail in Section 2.5. The resultant broadband waveforms modeled on the ground surface and predicted at depth are shown in Fig. 12 together with their Fourier and response spectra. Here, we show these synthetic broadband waveforms in the temporal domain in detail.

First, the dominant horizontal component of the broadband waveform modeled on the ground surface is shown in Fig. D1. Direct seismic phases Pg and Sg arrive in quick succession followed by the later SmS phase. The strongest amplitudes of both acceleration and velocity are generated by the Sg phase (PGA = 310.9 cm/s^2 and PGV = 18.04 cm/s). Next, we show an evolvement of the Arias intensity [30] calculated as

$$I_A(t) = \frac{\pi}{2g}\int_0^T a^2(t)\,\mathrm{d}t, \tag{D.1}$$

in which $I_A(t)$ is the Arias intensity, $a(t)$ is the acceleration waveform, g is the acceleration due to Earth's gravity, T is the total duration of the whole signal, and t denotes time. The 5th and 95th percentiles of the Arias intensity trace are commonly used for the definition of the earthquake strong-motion duration, while its maximum value is a measure of the strength of ground motions. In the case of the broadband waveform modeled on the ground surface, the strong-motion duration is about 3 s and the strength of the ground motion has the value of 49.48 cm/s.

Second, the dominant horizontal component of the broadband waveform predicted at the 153 m depth is shown in Fig. D2. It is predicted from the synthetic broadband waveforms modeled on the ground surface by using the SM at the BOBI site (Section 3.3) and the predictive TF from equation (4). All seismic phases have smaller amplitudes at depth than on the ground (PGA = 64.8 cm/s^2 and PGV = 7.53 cm/s). In terms of the Arias intensity, the strong-motion duration at the depth is about 3.3 s and the strength of the ground motion has the value of 2.839 cm/s.

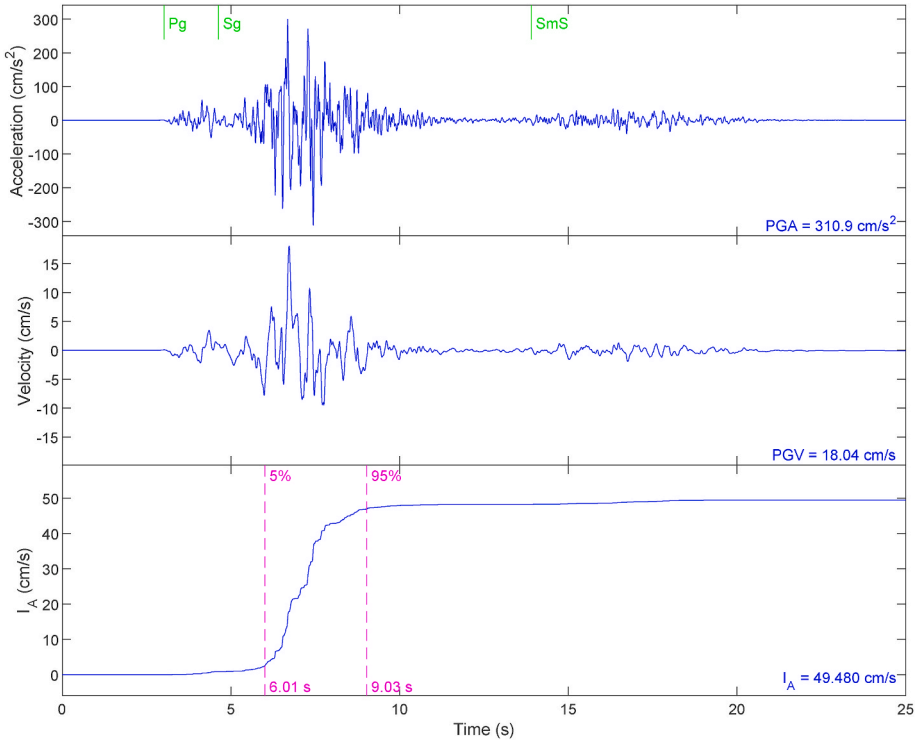


Fig. D1. Synthetic broadband waveform of the M_w5.8 earthquake scenario modeled on the ground surface at the BOBI site (Joyner-Boore distance 5 km; v_{S30} of 581 m/s). It shows the acceleration, velocity, and Arias intensity of the dominant horizontal component. This figure extends Fig. 12a.

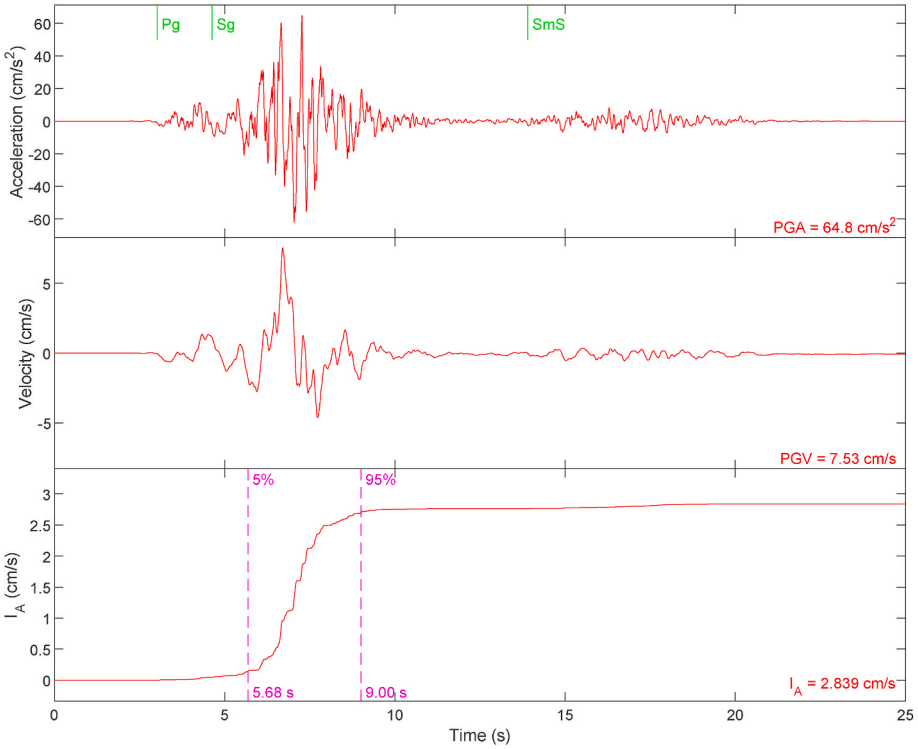


Fig. D2. Synthetic broadband waveform of the M_w5.8 earthquake scenario predicted at 153 m depth at the BOBI site (Joyner-Boore distance 5 km). It shows the acceleration, velocity, and Arias intensity for the dominant horizontal component of the ground motion at depth. This figure extends Fig. 12b.

Appendix E. Frequency-to-period conversion

In figures with surface-borehole TFs, we use frequencies in Hz on the *x*-axis, while the standard way of presenting spectra in civil engineering is to use periods in seconds. Mathematically, the period is simply the reciprocal of the frequency. Nevertheless, for the reader's convenience, we include the frequency-to-period conversion for frequencies used in this paper in Table E1.

Table E1
Frequency-to-period conversion.

Frequency (Hz)	0.3	0.5	1	3	5	10	40
Period (s)	3.33	2	1	0.33	0.2	0.1	0.025

References

[1] CEN. Eurocode 8: design of structures for earthquake resistance – Part 1: general rules, seismic actions and rules for buildings. EN 1998-1. Brussels, Belgium: European Committee for Standardization; 2004.
[2] SIA. SIA 261 Einwirkungen auf Tragwerke. Zurich, Switzerland: Société Suisse des ingénieurs et des architectes; 2020.
[3] Hadley DM, Helmberger DV. Simulation of strong ground motions. Bull Seismol Soc Am 1980;70:617–30. https://doi.org/10.1785/BSSA0700020617.
[4] Irikura K. Semi-empirical estimation of strong ground motions during large earthquakes. Bull Disast Prev Res Inst Kyoto Univ 1983;33:63–104.
[5] Fäh D, Suhadolc P, Mueller St, Panza GF. A hybrid method for the estimation of ground motion in sedimentary basins: quantitative modeling for Mexico City. Bull Seismol Soc Am 1994;84:383–99. https://doi.org/10.1785/BSSA0840020383.
[6] Hartzell S, Harmsen S, Frankel A, Larsen S. Calculation of broadband time histories of ground motion: comparison of methods and validation using strong-ground motion from the 1994 Northridge earthquake. Bull Seismol Soc Am 1999;89:1484–504. https://doi.org/10.1785/BSSA0890061484.
[7] Oprsal I, Zahradník J. Three-dimensional finite difference method and hybrid modeling of earthquake ground motion. J Geophys Res 2002;107. https://doi.org/10.1029/2000JB000082. ESE2-1-ESE-2-16.
[8] Graves RW, Pitarka A. Broadband ground-motion simulation using a hybrid approach. Bull Seismol Soc Am 2010;100:2095–123. https://doi.org/10.1785/0120100057.
[9] Mai PM, Imperatori W, Olsen KB. Hybrid broadband ground motion simulations: combining long-period deterministic synthetics with high frequency multiple S-to-S back-scattering. Bull Seismol Soc Am 2010;100:2124–42. https://doi.org/10.1785/0120080194.
[10] Aki K. Scaling law of seismic spectrum. J Geophys Res 1967;72:1217–31.
[11] Brune JN. Tectonic stress and the spectra of seismic shear waves from earthquakes. J Geophys Res 1970;75:4997–5009. https://doi.org/10.1029/JB075i026p04997.
[12] Ji C, Archuleta RJ. Two empirical double-corner-frequency source spectra and their physical implications. Bull Seismol Soc Am 2021;111:737–61. https://doi.org/10.1785/0120200238.
[13] Aki K. Attenuation of shear-waves in the lithosphere for frequencies from 0.05 to 25 Hz. Phys Earth Planet In 1980;21:50–60. https://doi.org/10.1016/0031-9201(80)90019-9.
[14] Cormier VF. The effect of attenuation on seismic body waves. Bull Seismol Soc Am 1982;72:S169–200. https://doi.org/10.1785/BSSA07206B0169.
[15] Bergamo P, Hammer C, Fäh D. On the Relation between empirical amplification and proxies measured at Swiss and Japanese stations: systematic regression analysis and neural network prediction of amplification. Bull Seismol Soc Am 2021;111:101–20. https://doi.org/10.1785/0120200228.
[16] Borcherdt RD. Effects of local geology on ground motion near San Francisco Bay. Bull Seismol Soc Am 1970;60:29–61. https://doi.org/10.1785/BSSA0600010029.
[17] Kanai K, Tanaka T, Yoshizawa S. Comparative studies of earthquake motions on the ground and underground. Bull Earthq Res Inst Univ Tokyo 1959;37:53–87. https://doi.org/10.15083/0000033900.
[18] Archuleta RJ, Seale SH, Sangas PV, Baker LM, Swain ST. Garner Valley downhole array of accelerometers: instrumentation and preliminary data analysis. Bull Seismol Soc Am 1992;82:1592–621. https://doi.org/10.1785/BSSA0820041592.
[19] Bonilla LF, Steidl JH, Gariel JC, Archuleta RJ. Borehole response studies at the garner valley downhole array, southern California. Bull Seismol Soc Am 2002;92:3165–79. https://doi.org/10.1785/0120010235.
[20] Shearer PM, Orcutt JA. Surface and near-surface effects on seismic-waves—theory and borehole seismometer results. Bull Seismol Soc Am 1987;77:1168–96. https://doi.org/10.1785/BSSA0770041168.
[21] Satoh T, Kawase H, Sato T. Evaluation of local site effects and their removal from borehole records observed in the Sendai region, Japan. Bull Seismol Soc Am 1995;85:1770–89. https://doi.org/10.1785/BSSA0850061770.
[22] Thompson EM, Baise LG, Kayen RE, Guzina BB. Impediments to predicting site response: seismic property estimation and modeling simplifications. Bull Seismol Soc Am 2009;99:2927–49. https://doi.org/10.1785/0120080224.
[23] Kramer SL. Geotechnical earthquake engineering. Upper Saddle River, New Jersey: Prentice Hall; 1996.
[24] Schnabel PB, Lysmer J, Seed HB. SHAKE: a computer program for earthquake response analysis of horizontally layered sites. Technical Report Rept. EERC 72-12. Berkeley, California: Earthquake Engineering Research Center, University of California; 1972.
[25] Hallo M, Bergamo P, Fäh D. Stochastic model to characterize high-frequency ground motion at depth validated by KiK-net vertical array data. Bull Seismol Soc Am 2022;112:1997–2017. https://doi.org/10.1785/0120220038.
[26] Bard P-Y, Bouchon M. The seismic response of sediment-filled valleys. Part 1. The case of incident SH waves. Bull Seismol Soc Am 1980;70:1263–86. https://doi.org/10.1785/BSSA0700041263.
[27] Sgattoni G, Castellaro S. Detecting 1-D and 2-D ground resonances with a single-station approach. Geophys J Int 2020;223:471–87. https://doi.org/10.1093/gji/ggaa325.
[28] Trifunac MD, Brady AG. On the correlation of seismic intensity scales with the peaks of recorded strong ground motion. Bull Seismol Soc Am 1975;65:139–62. https://doi.org/10.1785/BSSA0650010139.
[29] Reed JW, Kassawara RP. A criterion for determining exceedance of the operating basis earthquake. Nucl Eng Des 1990;123:387–96. https://doi.org/10.1016/0029-5493(90)90259-Z.
[30] Arias A. A measure of earthquake intensity. In: Hansen RJ, editor. Seismic design for nuclear power plants. Cambridge, Massachusetts: MIT Press; 1970.
[31] Archuleta RJ, Liu P, Steidl JH, Bonilla LF, Lavallée D, Heuze F. Finite-fault site-specific acceleration time histories that include nonlinear soil response. Phys Earth Planet In 2003;137:153–81. https://doi.org/10.1016/S0031-9201(03)00013-X.
[32] Power MS, Chang C-Y, Idriss IM, Kennedy RP. Engineering characterization of ground motion: task II: summary report (NUREG/CR-3805, 5. Washington, D.C: Office of Nuclear Regulatory Research, U.S. Nuclear Regulatory Commission; 1986.
[33] Sommaruga A, Eichenberger U, Marillier F. Seismic atlas of the Swiss Molasse Basin. In: The Swiss geophysical commission. Federal office of topography swisstopo. Switzerland: Wabern bei Bern; 2012.
[34] Poggi V, Edwards B, Fäh D. Characterizing the vertical-to-horizontal ratio of ground motion at soft-sediment sites. Bull Seismol Soc Am 2012;102:2741–56. https://doi.org/10.1785/0120120039.
[35] Diehl T, Clinton J, Cauzzi C, Kraft T, Kästli P, Deichmann N, Massin F, Grigoli F, Molinari I, Böse M, Hobiger M, Haslinger F, Fäh D, Wiemer S. Earthquakes in Switzerland and surrounding regions during 2017 and 2018. Swiss J Geosci 2021;114:4. https://doi.org/10.1186/s00015-020-00382-2.
[36] Wiemer S, Danciu L, Edwards B, Marti M, Fäh D, Hiemer S, Wössner J, Cauzzi C, Kästli P, Kremer K. Seismic hazard model 2015 for Switzerland (SUIhaz2015). Zurich, Switzerland: Swiss Seismological Service (SED) at ETH Zurich; 2016. https://doi.org/10.12686/a2.
[37] Bergamo P, Danciu L, Panzera F, Fäh D. Basis for the determination of waveforms for the sites of dams in Switzerland – subproject 1: disaggregation of seismic hazard for return periods of 1000, 5000, 10000 years. Technical Report SED 2021/11. Zurich, Switzerland: Swiss Seismological Service (SED) at ETH Zurich; 2021. https://doi.org/10.3929/ethz-b-000517545.
[38] Kanai K. Relation between the nature of surface layer and the amplitudes of earthquake motions. Bull Earthq Res Inst Univ Tokyo 1952;30:31–7. https://doi.org/10.15083/0000034123.
[39] Martin F, Kawase H, Modaressi A. Nonlinear soil response of a borehole station based on one-dimensional inversion during the 2005 Fukuoka prefecture western offshore earthquake. Bull Seismol Soc Am 2010;100:151–71. https://doi.org/10.1785/0120090125.
[40] Thompson EM, Baise LG, Tanaka Y, Kayen RE. A taxonomy of site response complexity. Soil Dynam Earthq Eng 2012;41:32–43. https://doi.org/10.1016/j.soildyn.2012.04.005.
[41] Régnier J, Bonilla L-F, Bertrand E, Semblat J-F. Influence of the VS profiles beyond 30 m depth on linear site effects: assessment from the KiK-net data. Bull Seismol Soc Am 2014;104:2337–48. https://doi.org/10.1785/0120140018.
[42] Kaklamanos J, Bradley BA. Challenges in predicting seismic site response with 1D analyses: conclusions from 114 KiK-net vertical seismometer arrays. Bull Seismol Soc Am 2018;108:2816–38. https://doi.org/10.1785/0120180062.
[43] Cadet H, Bard P-Y, Rodriguez-Marek A. Site effect assessment using KiK-net data: Part 1. A simple correction procedure for surface/downhole spectral ratios. Bull Earthq Eng 2012;10:421–48. https://doi.org/10.1007/s10518-011-9283-1.
[44] Olsen KB, Day SM, Bradley CR. Estimation of Q for long-period (>2 sec) waves in the Los Angeles basin. Bull Seismol Soc Am 2003;93:627–38. https://doi.org/10.1785/0120020135.
[45] Tarantola A, Valette B. Inverse problems = quest for information. J Geophys 1982;50:159–70.
[46] Hastings WK. Monte Carlo sampling methods using Markov chains and their applications. Biometrika 1970;57:97–109. https://doi.org/10.1093/biomet/57.1.97.
[47] Sambridge M. A Parallel Tempering algorithm for probabilistic sampling and multimodal optimization. Geophys J Int 2014;196:357–74. https://doi.org/10.1093/gji/ggt342.
[48] Maechling PJ, Silva F, Callaghan S, Jordan TH. SCEC Broadband Platform: system architecture and software implementation. Seismol Res Lett 2015;86:27–38. https://doi.org/10.1785/0220140125.
[49] Dreger DS, Beroza GC, Day SM, Goulet CA, Jordan TH, Spudich PA, Stewart JP. Validation of the SCEC Broadband Platform V14.3 Simulation methods using pseudospectral acceleration data. Seismol Res Lett 2015;86:39–47. https://doi.org/10.1785/0220140118.
[50] Goulet CA, Abrahamson NA, Somerville PG, Wooddell KE. The SCEC Broadband Platform validation exercise: Methodology for code validation in the context of

seismic-hazard analyses. Seismol Res Lett 2015;86:17–26. https://doi.org/10.1785/0220140104.
[51] Graves RW, Pitarka A. Refinements to the Graves and Pitarka (2010) broadband ground-motion simulation method. Seismol Res Lett 2015;86:75–80. https://doi.org/10.1785/0220140101.
[52] Zhu L, Rivera LA. A note on the dynamic and static displacements from a point source in multilayered media. Geophys J Int 2002;148:619–27. https://doi.org/10.1046/j.1365-246X.2002.01610.x.
[53] Razafindrakoto HNT, Cotton F, Bindi D, Pilz M, Graves RW, Bora S. Regional calibration of hybrid ground-motion simulations in moderate seismicity areas: application to the Upper Rhine Graben. Bull Seismol Soc Am 2021;111:1422–44. https://doi.org/10.1785/0120200287.
[54] Pousse G, Bonilla LF, Cotton F, Margerin L. Nonstationary stochastic simulation of strong ground motion time histories including natural variability: application to the K-Net Japanese database. Bull Seismol Soc Am 2006;96:2103–17. https://doi.org/10.1785/0120050134.
[55] Poggi V, Burjanek J, Michel C, Fäh D. Seismic site-response characterization of high-velocity sites using advanced geophysical techniques: application to the NAGRA-Net. Geophys J Int 2017;210:645–59. https://doi.org/10.1093/gji/ggx192.
[56] Panzera F, Alber J, Imperatori W, Bergamo P, Fäh D. Reconstructing a 3D model from geophysical data for local amplification modelling: the study case of the upper Rhone valley, Switzerland. Soil Dynam Earthq Eng 2022;155:107163. https://doi.org/10.1016/j.soildyn.2022.107163.
[57] Boore DM. Phase derivatives and simulation of strong ground motions. Bull Seismol Soc Am 2003;93:1132–43. https://doi.org/10.1785/0120020196.
[58] Konno K, Ohmachi T. Ground-motion characteristics estimated from spectral ratio between horizontal and vertical components of microtremor. Bull Seismol Soc Am 1998;88:228–41. https://doi.org/10.1785/BSSA0880010228.
[59] Poggi V, Fäh D. Report on site characterization for Böbikon, Switzerland (BOBI). Zurich, Switzerland: Swiss Seismological Service (SED) at ETH Zurich; 2014.
[60] Poggi V, Kleinbrod U, Fäh D. Report on site characterization for Hämikon, Switzerland (HAMIK). Zurich, Switzerland: Swiss Seismological Service (SED) at ETH Zurich; 2014.
[61] Poggi V, Michel C, Fäh D. Report on site characterization for Stiegenhof-Oberembrach (STIEG). Zurich, Switzerland: Swiss Seismological Service (SED) at ETH Zurich; 2013.
[62] Gruner U. Lyss (LK 1146), cross-section 3. In: Geologischer atlas der Schweiz 1: 25000; 2012. Federal Office of Topography swisstopo. Available at, https://data.geo.admin.ch/ch.swisstopo.geologie-geologischer_atlas_profile/profile/GA25_076_Plate_I_Section_3.pdf. [Accessed 26 September 2022].
[63] Zaugg A. Romanshorn (LK 1055), cross-section A. In: Geologischer atlas der Schweiz 1:25000; 2008. Federal Office of Topography swisstopo. Available at, https://data.geo.admin.ch/ch.swisstopo.geologie-geologischer_atlas_profile/profile/GA25_125_Plate_I_Section_A.pdf. [Accessed 26 September 2022].
[64] Swiss Seismological Service (SED) at ETH Zurich. The site characterization database for seismic stations in Switzerland, ETH Zurich. 2015. https://doi.org/10.12686/SED-STATIONCHARACTERIZATIONDB.
[65] Chieppa D, Hobiger M, Nagashima F, Kawase H, Fäh D. Identification of subsurface structures using H/V curves from earthquake recordings: application to seismic stations in Switzerland. Pure Appl Geophys 2023;180:755–87. https://doi.org/10.1007/s00024-022-03226-2.
[66] Wathelet M, Chatelain J-L, Cornou C, Di Giulio G, Guillier B, Ohrnberger M, Savvaidis A. Geopsy: a user-friendly open-source tool set for ambient vibration processing. Seismol Res Lett 2020;91:1878–89. https://doi.org/10.1785/0220190360.
[67] Nagashima F, Kawase H. The relationship between Vs, Vp, density and depth based on PS-logging data at K-NET and KiK-net sites. Geophys J Int 2021;225:1467–91. https://doi.org/10.1093/gji/ggab037.
[68] Jeong S-H, Lee K-H, Jang W-S. PRISM for Earthquake Engineering: a Program for seismic response analysis of SDOF systems, Version 2.0.0. Incheon, South Korea: Earthquake Engineering Research Group at the INHA University; 2015.
[69] Nash JE, Sutcliffe JV. River flow forecasting through conceptual model. Part 1 — a discussion of principles. J Hydrol 1970;10:282–90. https://doi.org/10.1016/0022-1694(70)90255-6.
[70] Poggi V, Edwards B, Fäh D. Derivation of a reference shear-wave velocity model from empirical site amplification. Bull Seismol Soc Am 2011;101:258–74. https://doi.org/10.1785/0120100060.
[71] Campus P, Fäh D. Seismic monitoring of explosions: a method to extract information on the isotropic component of the seismic source. J Seismol 1997;1: 205–18. https://doi.org/10.1023/A:1009781722363.
[72] Lanza F, Diehl TC, Eberhart-Phillips D, Herwegh M, Fäh D, Wiemer S (2024) Crustal seismic attenuation structure of the Central Alps and their foreland from local earthquakes. [in prep].
[73] Swiss Seismological Service (SED) at ETH Zurich. National seismic networks of Switzerland. ETH Zurich; 1983. https://doi.org/10.12686/SED/NETWORKS/CH.
[74] MathWorks. MATLAB version 9.10.0.1602886 (R2021a). Natick, Massachusetts: The MathWorks, Inc.; 2021.
[75] Wessel P, Luis JF, Uieda L, Scharroo R, Wobbe F, Smith WHF, Tian D. The generic mapping Tools version 6. G-cubed 2019;20:5556–64. https://doi.org/10.1029/2019GC008515.